Experimental study on static and dynamic properties of fly ash-slag based strain-hardening geopolymer composites

Yi Wang, Hui Zhong, Mingzhong Zhang*

Department of Civil, Environmental and Geomatic Engineering, University College London, London, WC1E 6BT, UK

Abstract: Strain-hardening geopolymer composite (SHGC) is a special group of fibre reinforced geopolymer composites, which exhibits ultra-high ductility and multiple microcracks under tension. This paper presents an experimental study on the effect of polyvinyl alcohol (PVA) fibre content (0%, 1%, 1.5%, and 2%) on engineering properties of fly ash-slag based SHGC cured at ambient temperature in terms of flowability, drying shrinkage and mechanical properties, with a special focus on strain-hardening behaviour and dynamic compressive behaviour. Single-crack tension test and three-point bending test were conducted to determine the micromechanical properties of SHGC, dynamic properties of which were explored using Split Hopkinson pressure bar. Results indicate that the flowability, drying shrinkage and compressive strength of SHGC reduce with the increase of PVA fibre content, while the tensile strength and ultimate strain of SHGC under uniaxial tension are significantly improved because of the fibre bridging effect. The dynamic compressive behaviour of SHGC is strongly associated with the strain rate. The dynamic compressive strength of SHGC with various PVA fibre dosages is increased by 9.26-29.97% and 41.59-69.78% as the strain rate increases from 50 s^{-1} to 100 s^{-1} and 150 s^{-1}, respectively. Overall, the mixture containing 1.5% PVA fibre can be regarded as the optimal mixture for SHGC considering static mechanical properties and dynamic compressive behaviour.

Keywords: Engineered geopolymer composites; Strain-hardening behaviour; Multiple micro-cracking; Micromechanics; Dynamic impact factor; Toughening mechanism

1. Introduction

In the past few decades, intensive infrastructure constructions around the world have led to a dramatic consumption of ordinary Portland cement (OPC) [1], the production of which accounts for around 8% of global carbon emissions annually as the production of 1 tonne OPC generates 0.7-1.1 tonnes of carbon emissions [2, 3]. To tackle this issue, it is vital to find eco-friendly binders as alternatives to OPC for concrete infrastructures. Geopolymers (also known as alkali-activated materials) that are

* Corresponding author. E-mail address: mingzhong.zhang@ucl.ac.uk (M. Zhang)

produced by industrial or agricultural by-products such as fly ash, ground granulated blast-furnace slag, silica fume, and rice husk ash have attracted increasing attention and been increasingly used as alternatives to OPC because of low energy consumption, reduced greenhouse emissions, and superior mechanical properties, thermal performance and durability [4]. Using geopolymer as a substitute for OPC in concrete can help reduce the CO_2 emission of concrete by 55-75% [5]. Meanwhile, the usage of geopolymers made of industrial by-products or wastes could reduce the burden of the natural environment and the consumption of natural limestone required for manufacturing OPC.

Geopolymers are brittle and prone to cracking under tensile or flexural stress, which impairs their engineering properties and durability. To control the cracking and enhance the overall performance of geopolymers, different types of short fibre such as steel fibre [6, 7], carbon fibre [8, 9], synthetic fibre [10, 11], and natural fibre [12, 13] are incorporated into geopolymers to develop high-performance fibre reinforced geopolymer composites. Strain-hardening geopolymer composite (SHGC) is a new class of fibre reinforced geopolymer composites, which exhibits the tensile strain-hardening behaviour with ultra-high tensile strain capacity and multiple microcracks with an average crack width of around 60 μm [14, 15]. The sequential formation of multiple microcracks on SHGC specimens indicates the strain-hardening behaviour, which is governed by the strength and energy criteria that the tensile cracking strength of matrix must be no higher than the fibre bridging strength and the crack tip toughness (J_{tip}) must not exceed the complementary energy of the bridging fibres (J_b'), according to micromechanics theory [16]. Because of the significant tensile strain capacity and self-controlled tight cracks, SHGC can be used in different civil infrastructures, especially those subjected to extreme loadings such as earthquakes, impacts, and blasts.

In recent years, an increasing number of studies have been focused on the development and investigation of engineering properties of SHGC made from different industrial by-products, among which fly ash and slag are the most widely used precursors to produce SHGC because of the low cost and wide availability of them [17]. It is worth noting that most existing studies are focused on pure fly ash or slag based SHGC, which have some drawbacks that fly ash-based geopolymer requires heat curing to gain acceptable early age strength, whereas slag-based geopolymer has poor workability, rapid setting and high shrinkage [18]. To address these limitations, there has been an increasing interest in the development of blended fly ash-slag based SHGC, which can achieve the desired engineering properties when cured at ambient conditions and thus would have wide applications [19, 20]. For instance, Nematollahi et al. [21, 22] studied the strain-hardening behaviour of fly ash-slag

based SHGC reinforced with PVA and PE fibres. They concluded that the ambient-cured SHGC has a comparable tensile strength (4.7 MPa) and tensile strain capacity (4.2%), while the energy consumption and carbon emissions of SHGC were 36% and 76% less than the OPC-based counterpart, i.e., strain-hardening cementitious composites. The effects of PE fibre content (0%, 0.5%, 0.75%, 1%, 1.5%, and 2% by volume) and curing conditions (ambient curing and heat curing) on strain-hardening behaviour of SHGC were explored by Shaikh et al. [23], who observed that the ambient-cured SHGC outperformed the heat-cured SHGC in terms of ductility and the SHGC specimens containing 0.75-1% PE fibre can be regarded as the optimal mixture considering the strain-hardening behaviour. Nedeljković et al. [24] developed the ductile geopolymer composite and applied it in casting a large-scale canoe, which demonstrated the potential of SHGC in large-scale engineering applications such as structural elements, bridges, and other engineering structures. Ling et al. [25] investigated the effect of slag replacement ratio (0%, 10%, 20%, and 30% by weight) on uniaxial tensile behaviour of PVA fibre reinforced fly ash-based SHGC and found that the increase of slag content enhanced the strengths but reduced the ductility and toughness of SHGC due to the increased density of matrix and fibre-matrix bond strength. The optimum replacement ratio of fly ash with slag was found to be 20%. Nevertheless, the effects of content and length of PVA fibre on the engineering properties of blended fly ash-slag based SHGC have not been extensively studied to date, and most existing studies are focused on static mechanical properties of SHGC, while the dynamical mechanical properties of SHGC have been rarely investigated. To the best of the authors' knowledge, there is only one literature available on this subject, which explored the dynamic properties of metakaolin-based SHGC reinforced with either PVA fibre or ultra-high molecular-weight polyethylene (UHMWPE) fibre using a gravity-driven split Hopkinson tension bar at strain rates of up to 300 s^{-1} [26]. It was concluded that SHGC containing UHMWPE fibre outperformed the PVA fibre reinforced SHGC under quasi-static and impact tensile loads because of the relatively higher tensile strength and elastic modulus, but UHMWPE fibre is much more expensive than PVA fibre. However, a systematic study on dynamic properties of fly ash-slag based SHGC is still lacking, which would hinder its engineering applications.

The main purpose of this paper is to provide a comprehensive understanding of the effect of PVA fibre on engineering properties of fly ash-slag based SHGC cured at ambient temperature, with a special focus on static tensile behaviour and dynamic compressive behaviour. A series of tests were conducted on SHGC containing various fibre volume fractions (0%, 1%, 1.5%, and 2%) to measure their engineering properties including flowability, drying shrinkage, tensile properties, strain-

hardening behaviour, and static and dynamic compressive behaviour. The effects of PVA fibre content on these engineering properties of SHGC were then estimated, based on which the toughening mechanism was explored, and the optimal mix proportion for SHGC was obtained.

2. Experimental program

2.1 Raw materials

In this study, geopolymers were synthesised using low-calcium fly ash (equivalent to ASTM Class F [27]) and ground granulated blast-furnace slag as precursors, the chemical compositions and particle size distribution of which are presented in **Table 1** and **Fig. 1**, respectively. The specific gravities of fly ash and slag are 2.19 and 2.90, and the average particle sizes of them are 19.58 μm and 9.78 μm, respectively. A mixture of 10 M sodium hydroxide (SH) solution and sodium silicate (SS) solution with modulus (SiO_2:Na_2O ratio) of 2.0 was used as alkaline activator. The SH solution was prepared by dissolving the SH powder in the tap water and then stored in the cupboard until its temperature became ambient. This allows the heat dissipation caused by the exothermic chemical reaction in the mixed solution [25]. As per a previous study [28], the modified polycarboxylate-based superplasticiser (SP) (Sika ViscoFlow 3000) was added to improve the workability of SHGC and ensure a uniform fibre dispersion in SHGC.

Fine silica sand was used as aggregate, which has a specific gravity of 2.66 and a maximum and mean particle size of 250 μm and 130 μm, respectively. The particle size distribution of fine silica sand is also shown in **Fig. 1**. The sand was used in surface saturated dry (SSD) condition with an absorption rate of zero, according to a preliminary absorption test. PVA fibre coated by 1.2 wt% oil to control fibre-matrix interface properties, supplied by Kuraray, Japan, was used to produce SHGC. The physical and mechanical properties of PVA fibre are presented in **Table 2**.

Table 1 Chemical compositions (wt%) of fly ash (FA) and ground granulated blast-furnace slag (GGBS).

Oxide	SiO_2	Al_2O_3	CaO	MgO	K_2O	Fe_2O_3	TiO_2	Na_2O	SO_3	LOI
FA	57.02	32.35	2.88	0.58	2.07	3.01	1.26	0.03	0.41	0.39
GGBS	31.85	17.31	41.20	6.13	0.33	0.34	0.62	0.03	1.78	0.41

Note: LOI (loss on ignition).

Table 2 Physical and mechanical properties of polyvinyl alcohol (PVA) fibre.

Fibre ID	Length (mm)	Nominal diameter (μm)	Aspect ratio	Density (g/cm^3)	Tensile strength (MPa)	Elastic modulus (GPa)
PVA	12	40	300	1.3	1600	41

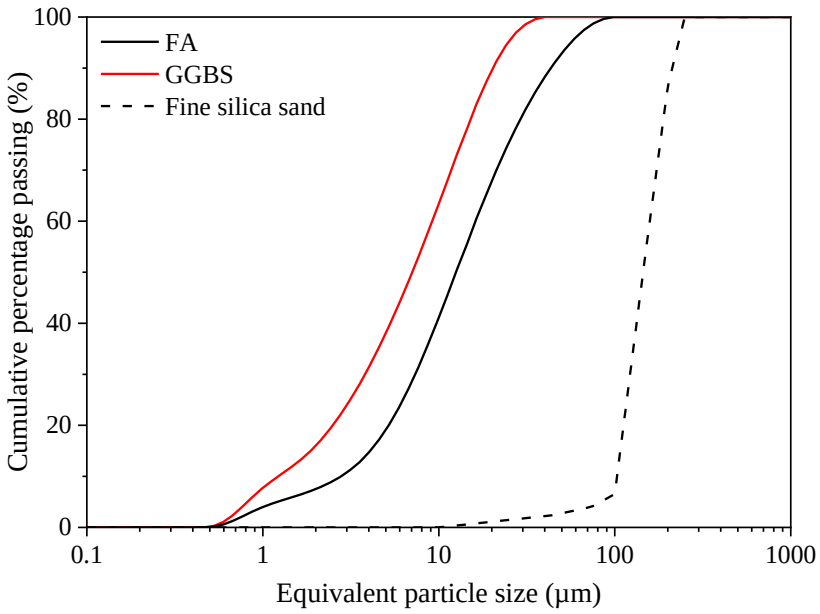

Fig. 1. Particle size distribution of fly ash, slag, and fine silica sand.

2.2 Mix proportions

Table 3 shows the mix proportions of SHGC. Based on a previous study [28], the geopolymer binders were prepared with the fly ash/slag ratio of 0.8:0.2, SS/SH solution ratio of 2.0, and sand/binder ratio of 0.2. To ensure the flowability of the mix, the alkaline activator/binder ratio and SPs/binder ratio were determined as 0.45 and 0.01, respectively, where the activator/binder ratio denotes the weight ratio of alkaline activator composed of SH and SS solution to geopolymer binder consisting of fly ash and slag. No additional water was added. Herein, the studied parameter was the content of PVA fibre. For the mixture labels given in **Table 3**, "P" represents PVA fibre, and the denoted number stands for the fibre content. For instance, P0 represents the mixture without fibre, and P2 denotes the mixture containing 2% PVA fibre. All specimens were prepared following the same procedure introduced in Section 2.3.

Table 3 Mix proportions of SHGC.

Mix No.	Binder		Activator/binder	Sand/binder	SPs/binder	PVA (vol%)
	FA	GGBS				
P0	0.8	0.2	0.45	0.2	0.01	0
P1	0.8	0.2	0.45	0.2	0.01	1.0
P1.5	0.8	0.2	0.45	0.2	0.01	1.5
P2	0.8	0.2	0.45	0.2	0.01	2.0

2.3 Specimen preparation

All SHGC specimens were prepared using a 10 L Hobart mixer, following the preparation steps

described in a previous study [28], with appropriate adjustment considering the differences of raw materials. The entire mixing process typically lasted approximately 8 min and 30 s. Firstly, all solid ingredients (FA, GGBS, and sand) were added to the mixer and dry mixed for 1.5 min until a homogeneous mix was obtained. Then, the alkaline activator was slowly added into the dry mixture to avoid the rapid setting and this process lasted for about 3 min. Afterwards, SPs were added to achieve an appropriate flowability and mixed for another 1 min. PVA fibres were then slowly incorporated into the mixture by rubbing and separating fibres to reduce the multifilament forms, followed by the mixing of the whole mixture for another 1 min. The fresh SHGC was poured into the moulds immediately after the mixing and then vibrated to allow the air bubble to escape and compact the SHGC. All specimens were covered with cling films to prevent moisture loss after casting and stored in the ambient environment for 24 h. Then, the specimens were demoulded and stored in a standard curing room at an average temperature of 20 ± 2 °C and relative humidity of 95% until the testing ages.

2.4 Test methods

2.4.1 Flow table test

Flow table test was conducted in accordance with ASTM C1437-15 [29] to determine the flowability of SHGC by measuring the spread diameter of fresh mortar immediately after mixing. The truncated mould with a top diameter of 70 mm, a bottom diameter of 100 mm (D_0 = 100 mm) and a depth of 50 mm was filled with fresh SHGC on the wet flow table. The mould was lifted upwards, and the table was dropped 25 times in 15 s. Four measurements of the diameter of each mixture were taken to obtain the average flow value, D (mm). The flow (F) of the fresh SHGC specimen can be calculated by $F = \frac{(D-D_0)}{D_0} \times 100\%$.

2.4.2 Drying shrinkage test

Drying shrinkage test was carried out on SHGC prisms with a dimension of 280 × 50 × 50 mm (length × width × height) as per ASTM C490-17 [30] on a daily basis. The prisms were exposed to the environment with a temperature of 20 ± 2 °C and relative humidity of 60 ± 5%. The changes in the length of specimens were measured using a digital gauge with an accuracy of ± 0.01 mm.

2.4.3 Uniaxial tension test

Uniaxial tension test was performed according to JSCE Recommendations [31] using a universal testing machine WDW-50E with a maximum loading capacity of 50 kN to determine the tensile properties and evaluate the strain-hardening behaviour of SHGC specimens. The uniaxial tensile

loading with the displacement control at a rate of 0.5 mm/min was imposed on the dog-bone shaped specimens at 28 d of curing, the dimension of which is displayed in **Fig. 2**. Two LVDTs (linear variable displacement transducers) were used and attached on both sides of the testing specimen, as illustrated in **Fig. 3**. The mean values of tensile strength and strain capacity of three specimens were obtained, and the cracking characteristics of specimens were captured to explore the failure mechanism after the uniaxial tension test.

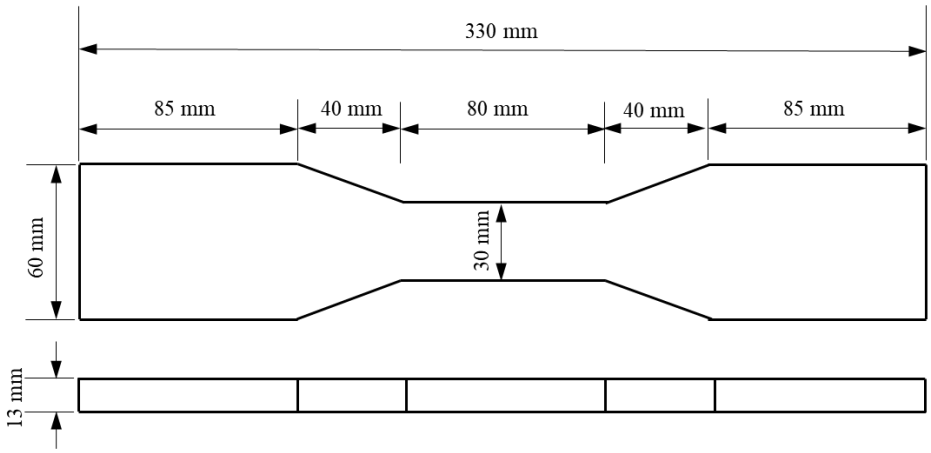

Fig. 2. Dimensions of the dog-bone shaped specimen for the uniaxial tension test.

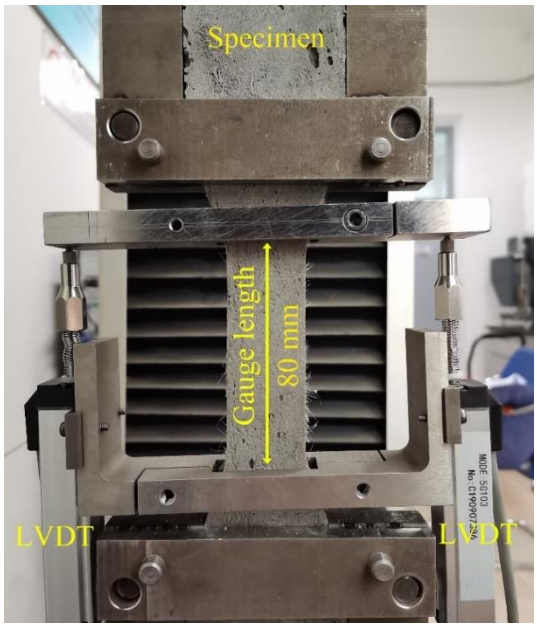

Fig. 3. Setup of the uniaxial tension test.

2.4.4 Single-crack tension test

Single-crack tension test was conducted on dog-bone shaped specimens using a universal testing machine WDW-50E with a maximum loading capacity of 50 kN to determine the maximum fibre bridging strength (σ_0) and the maximum available complementary energy (J_b') [32-34]. The dimensions of the specimens and the setup of the single-crack tension test were the same as those shown in **Figs. 2** and **3**, respectively. Two LVDTs were used and attached on both sides of the testing

specimen to measure the crack opening. Prior to testing, all specimens were cut with the diamond saw on the four faces in the centre to create the notch with the depth of 6.5 mm and 2 mm, respectively, as illustrated in **Fig. 4**, where the shaded and unshaded areas denote the remained area and the notched area, respectively. This was prepared to facilitate the formation of the single crack of specimens [33]. It is worth noting that the thickness of the notch was less than 0.6 mm [32, 33]. The mean values of three specimens at 28 d of curing were obtained.

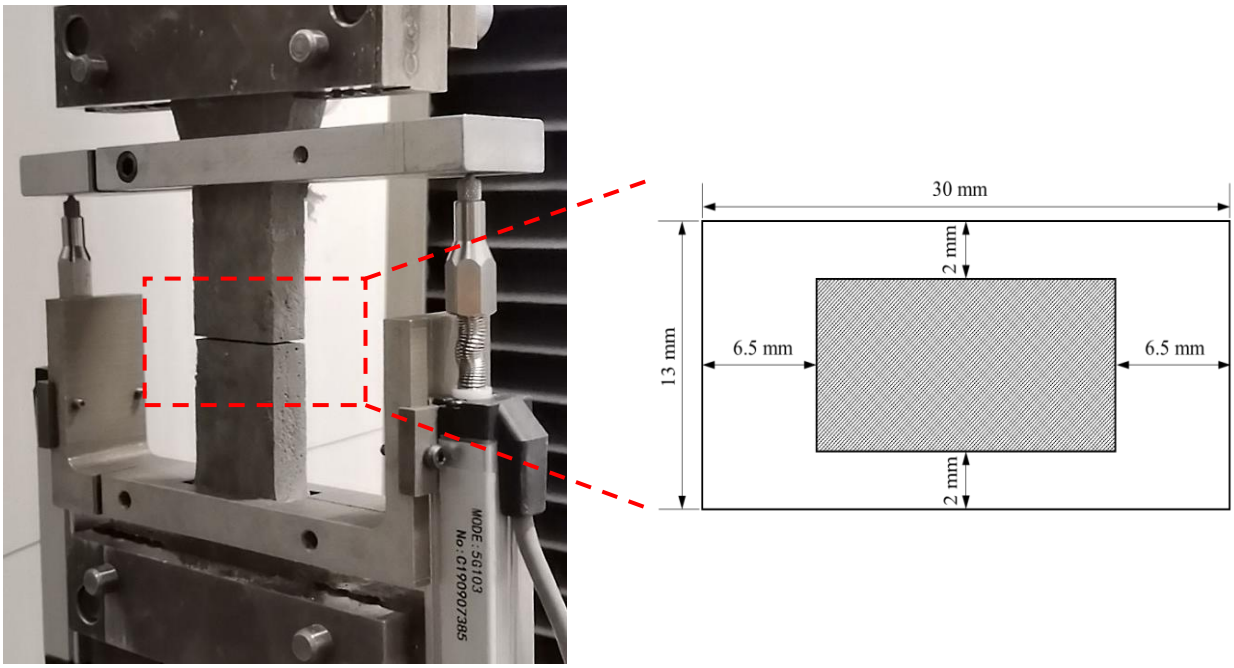

Fig. 4. Setup and schematic illustration of the notched specimen for the single-crack tension test.

2.4.5 Three-point bending test

Three-point bending test was carried out to evaluate the fracture toughness and crack tip toughness of the matrix according to ASTM E399-12 [35] using a universal testing machine WDW-50E with a maximum loading capacity of 50 kN. **Fig. 5** shows the setup of three-point bending test. Single-edge notched prismatic specimens with a dimension of 160 × 40 × 40 mm were prepared and used for testing after 28 d of curing. Prior to testing, the diamond cutting saw was used to prepare the notch with 16 mm in depth at the centre of the bottom surface. The relative notch depth ratio α ($\alpha = \frac{a}{W}$) was kept as 0.4 for all specimens (hereby a = 16 mm, W = 40 mm). The load span of specimens was 90 mm. The loading rate was 0.5 mm/min during the test. The ultimate loads were recorded, based on which the fracture toughness (K_m) and crack tip toughness (J_{tip}) of the matrix can be calculated using the peak load as follows [36]:

$$K_m = \frac{1.5P_{max}S\sqrt{\pi a}}{BW^2} \times f(\alpha) \quad (1)$$

$$f(\alpha) = \frac{(0.68-0.744\alpha)}{(1-2.155\alpha+1.161\alpha^2)} + 0.36 - 2.088\alpha + 4.611\alpha^2 - 6.499\alpha^3 + 4.232\alpha^4 \quad (2)$$

$$J_{tip} = K_m^2/E_m \quad (3)$$

where P_{max} is the peak load, B is the specimen width (mm), W is the specimen depth (mm), S is the loading span (mm), and a is the notch depth.

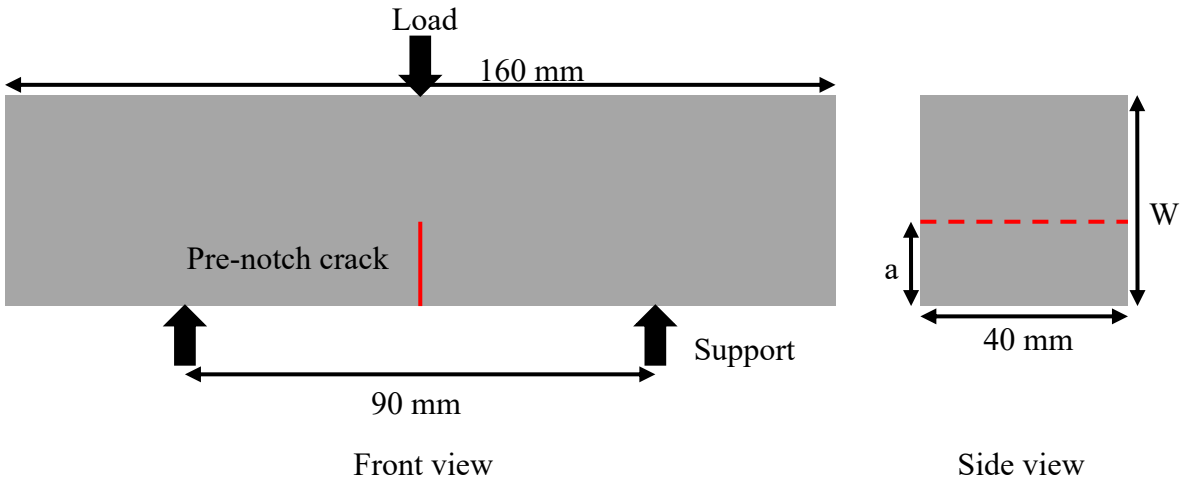

Fig. 5. Schematic illustration of three-point bending test setup (notch depth a = 16 mm, specimen depth W = 40 mm).

2.4.6 Static compression test

Static compression test was carried out according to ASTM C109-16 [37] on the specimens with the size of 50 × 50 × 50 mm. Given that the strength of concrete would be affected by the specimen size, many studies determined the dynamic increase factor (DIF) using the static and dynamic compressive strengths that were measured using the same specimen size [38-40]. Thus, cylindrical specimens with 100 mm diameter and 50 mm height were tested to estimate the DIF at various strain rates. All specimens were tested at 28 d using the machine CONTROLS C4600/FR with a maximum load capacity of 2000 kN. The loading rate was 1200 N/s. Three specimens were tested, and the mean value was considered as the compressive strength.

2.4.7 Split Hopkinson pressure bar (SHPB) test

Split Hopkinson pressure bar (SHPB) test was conducted to measure the dynamic compressive behaviour of SHGC at various strain rates. The SHPB machine used in this study was made of a superior alloy steel material and had a diameter of 100 mm, the lengths of bullet, incident, transmission, and absorbing bars of which were 600, 5000, 3500, and 1200 mm, respectively. Three cylindrical specimens with a diameter of 100 mm and a height of 50 mm were used to obtain the mean value of dynamic compressive properties of SHGC specimens at 28 d. The specimens were

sandwiched between the incident and transmission bars before the SHPB test, as illustrated in **Fig. 6**. To start the test, the start button on the computer system was clicked, and then the bullet started to be propelled by the compressed nitrogen. The incident bar was then impacted by the 100 mm bullet and the impact velocity was measured by the speed detection device shown in **Fig. 6**. Subsequently, an incident pulse ($\varepsilon_i(t)$) was produced and known as the incident wave. At the interface between the incident bar and the specimen, the incident wave was partially reflected from the specimen due to the impedance difference, which is known as reflected pulse ($\varepsilon_r(t)$) [41]. The remaining wave was transmitted through the specimen into the transmission bar called transmission pulse ($\varepsilon_t(t)$).

These strain pulses were recorded using two strain gauges (see **Fig. 6**) which were demonstrated in the form of strain against time. During the SHPB test, the pulse shaper with the size of 60 mm in diameter and 2 mm in height was mainly used to achieve the stress equilibrium to ensure the reliability and accuracy of SHPB test results [42, 43]. **Fig. 7** displays an example of checking the stress equilibrium. It can be observed that the sum of incident pulse and reflected pulse has a good match with the transmission pulse, which confirms that the stress equilibrium along the specimen thickness has been reached. The time histories of stress ($\sigma_s(t)$), strain ($\varepsilon_s(t)$), and strain rate ($\dot{\varepsilon}_s(t)$) were determined using the following equations [42]:

$$\sigma_s(t) = \frac{E_0 A_0}{2A_s}[\varepsilon_i(t) + \varepsilon_r(t) + \varepsilon_t(t)] \tag{4}$$

$$\varepsilon_s(t) = \frac{C_0}{l_s}\int_0^t [\varepsilon_i(t) - \varepsilon_r(t) - \varepsilon_t(t)]\, dt \tag{5}$$

$$\dot{\varepsilon}_s(t) = \frac{C_0}{l_s}[\varepsilon_i(t) - \varepsilon_r(t) - \varepsilon_t(t)] \tag{6}$$

where E_0 is the elastic modulus of the bars (MPa), A_0 is the cross-sectional area of the bars (mm^2), A_s is the cross-sectional area of the tested specimen (mm^2), C_0 is the longitudinal wave velocity of the bars (m/s), and l_s stands for the thickness of the tested specimen (mm).

The dynamic compressive behaviour of SHGC was investigated at different strain rates, which were produced by various impact velocities. Three groups of impact velocity were applied, including low impact velocity of around 6 m/s, medium impact velocity of about 8 m/s, and high impact velocity of approximately 10 m/s, which were used to differentiate the failure patterns of specimens from low strain rate to high strain rate.

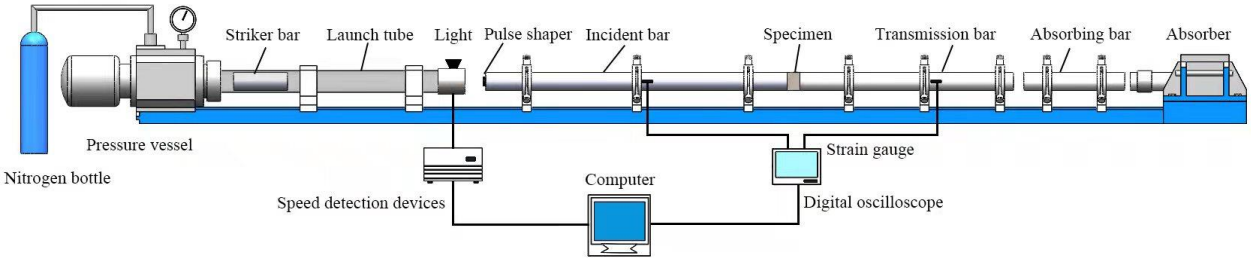

Fig. 6. Schematic diagram of splitting Hopkinson pressure bar (SHPB) testing system.

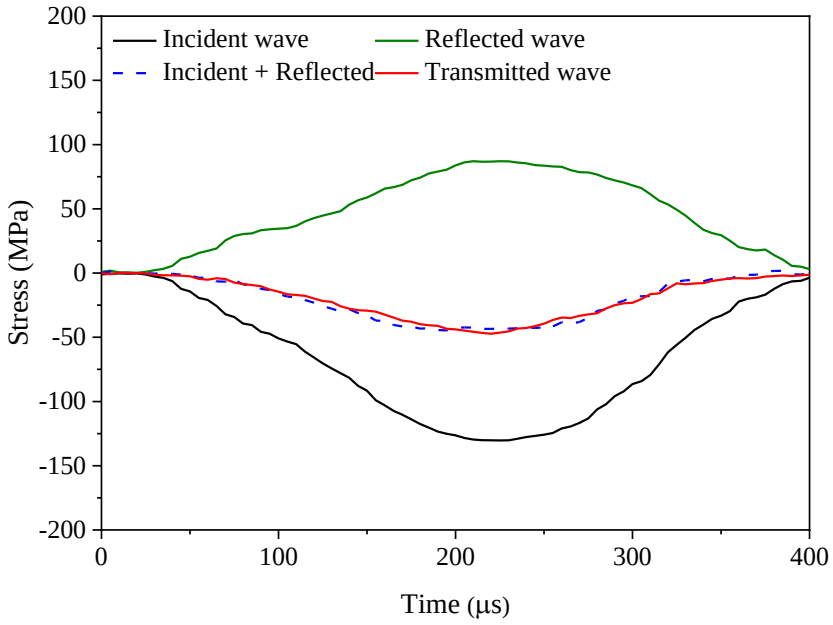

Fig. 7. An example of checking the stress equilibrium for SHPB test.

3. Results and discussion

3.1 Flowability

Fig. 8 shows the flow values of fresh SHGC mixtures with different fibre contents. Better workability can be reflected by higher flow value, and therefore the mix can be easier for casting and compacting. The flow values of fresh SHGC mixtures reduced with the increase of fibre content. The geopolymer mortar without fibre (P0) had a flow value of 94.66%. Compared to P0, when the fibre content was increased to 1%, 1.5%, and 2%, the flow value of the fresh mixture was reduced by 13.73%, 22.89%, and 26.06%, respectively. The reduction in flowability of SHGC with the increase of fibre content agrees well with that presented in [28, 44, 45], which can be ascribed to the contact mechanism between PVA fibres in geopolymer mortar [46]. Therefore, the overall movement of the fresh SHGC was confined, resulting in an increased shear resistance.

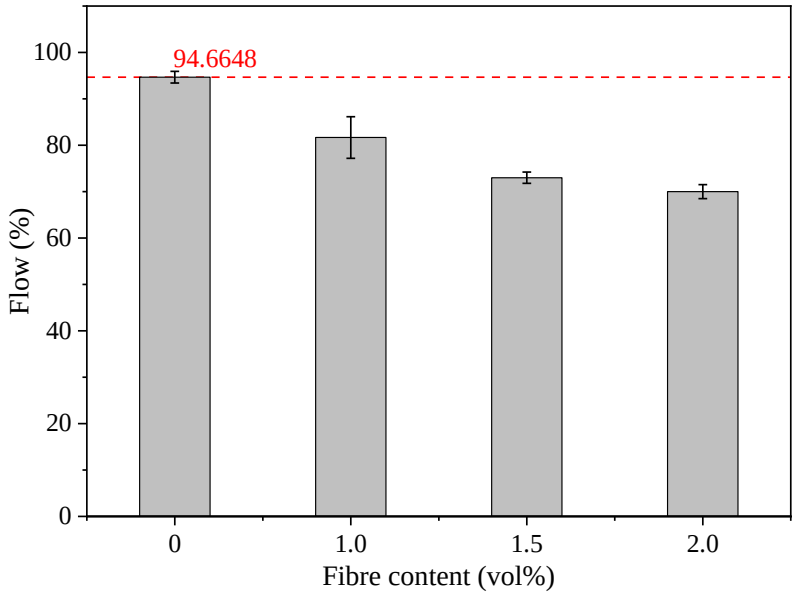

Fig. 8. Flowability of fresh SHGC specimens with various fibre content.

3.2 Drying shrinkage

Drying shrinkage is resulted from the loss of capillary water in hardening composites, which leads to deformation and cracks in structural elements [46]. **Fig. 9** illustrates the drying shrinkage of all mixtures with various fibre content. Overall, all specimens exhibited a sharp drop in shrinkage at early ages due to the evaporation of capillary water from internal (with higher relative humidity) to external environment (with lower relative humidity) through pore network of SHGC [47]. With the increase of curing age, the drying shrinkage reduced, which can be ascribed to the resistance of volume deformation of hardened SHGC induced by the rigid zeolite structure formed during geopolymerisation [47, 48].

Overall, the drying shrinkage of SHGC specimens at 28 d was decreased with the increase of fibre content, as shown in **Fig. 9**. The geopolymer mortar without fibre (P0) at 28 d had a drying shrinkage of -0.77%. In comparison with P0, the incorporation of PVA fibre by 1%, 1.5%, and 2% resulted in a reduction of drying shrinkage by 31.33%, 57.25%, and 48.84%, respectively. The addition of PVA fibre up to 1.5% resulted in a decrease in drying shrinkage because of the restriction effect by PVA fibre. As the fibre content increased from 1.5% to 2.0%, a rise in drying shrinkage of SHGC can be observed, which can be ascribed to the fibre corrugation and weak fibre-matrix interface due to the poor compaction of the composites and weak interaction between fibre and matrix. The weak interaction could lead to debonding by expanding the gap between fibre and its surrounding matrix, which curtailed the stress transfer in SHGC specimens and reduced the resistance to shrinkage

[49]. Moreover, the excessive addition of PVA fibre can result in poor compaction and higher porosity of SHGC, where the formed pore network allows the moisture to move towards the surface of specimens [46, 50, 51].

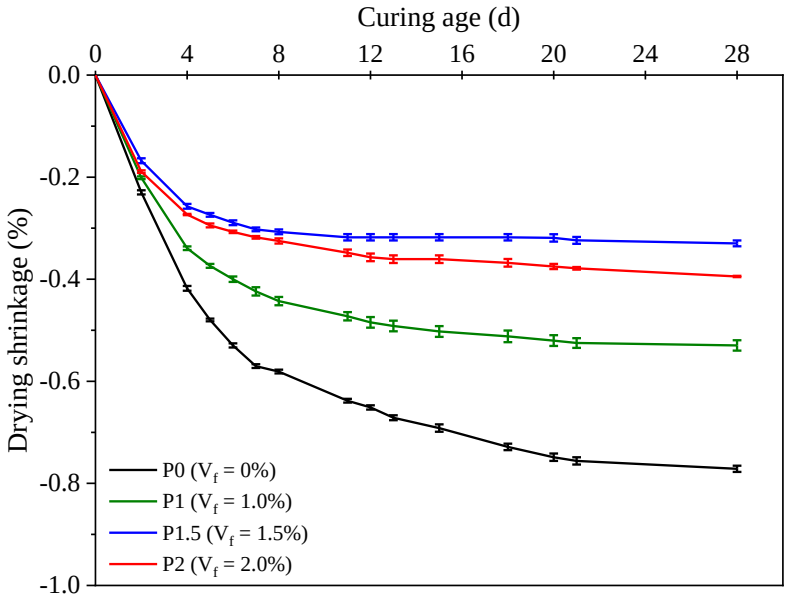

Fig. 9. Drying shrinkage of SHGC specimens with various fibre content (error bars denote standard deviations).

3.3 Strain-hardening behaviour

This section presents the results of the static uniaxial tension test on SHGC specimens with various fibre content, including stress-strain response, failure patterns, tensile strength, and micromechanical analysis. **Table 4** summarises the uniaxial tensile properties of all mixtures.

Table 4 Uniaxial tensile performance of all mixtures.

Mix No.	Fist-crack strength (MPa)	Ultimate tensile strength (MPa)	Tensile strain capacity (%)	Average crack width (μm)
P0	-	1.04	0.03	-
P1	1.13	2.61	3.75	142.86
P1.5	1.84	4.37	5.15	111.35
P2	2.68	4.45	4.91	85.39

3.3.1 Stress-strain response

Fig. 10 displays the uniaxial tensile stress-strain curves of all mixtures. Due to the unexpected failure of one out of three specimens for P0 and P1 before test setup, the stress-strain response of two specimens is presented for them, while three specimens were adopted for P1.5 and P2. The reference mixture (P0) exhibited a brittle failure and failed immediately after the crack initiated in the specimen at the elastic stage, while all SHGC specimens demonstrated strain-hardening behaviour under

uniaxial tension. For SHGC specimens, the tensile stress increased linearly with the increase of tensile strain until it reached the first-crack strength. Then, the stress-strain curves became non-linear, and the slope of the curve decreased significantly, suggesting that the specimens entered the strain-hardening stage. Finally, the maximum tensile stress was reached, and the specimens failed.

As seen in **Fig. 10** and **Table 4**, P0 had an ultimate tensile strain of 0.03%, and the incorporation of fibres significantly enhanced the tensile strain capacity of the material. For SHGC specimens, the content of the incorporated PVA fibres had a significant influence on the stress-strain response of SHGC specimens in terms of first-crack strength, strain-hardening stage, and ultimate strain. SHGC specimens reinforced with 1% fibre had a first-crack strength of 1.13 MPa, and an ultimate strain of 3.75%. The strain-hardening stage experienced obvious serrated lines due to the continuous crack initiation and propagation up to failure, which represented comparatively wider cracks. When the fibre content was increased to 1.5%, the first-crack strength and ultimate strain of SHGC specimens were increased by 62.30% and 37.30%, respectively. SHGC specimens with 2% fibre (P2) had a fist-crack strength of 2.68 MPa, which was 45.72% higher than that of P1.5, while its tensile strain was 4.89% lower than that of P1.5. As compared with P0, SHGC specimens reinforced with various fibre content resulted in the ultimate tensile strain capacity of 147-201 times that of P0, which can be attributed to the fibre-bridging effect.

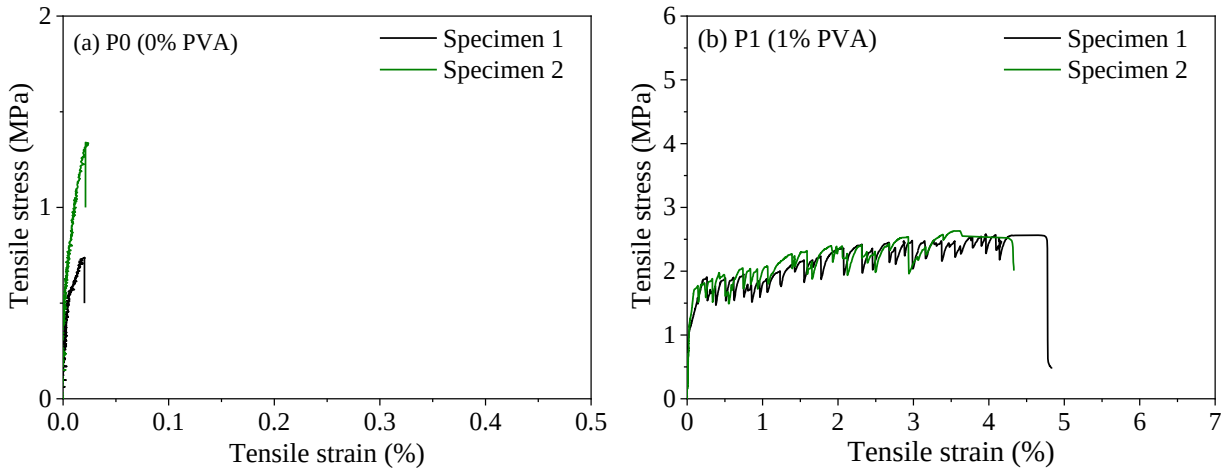

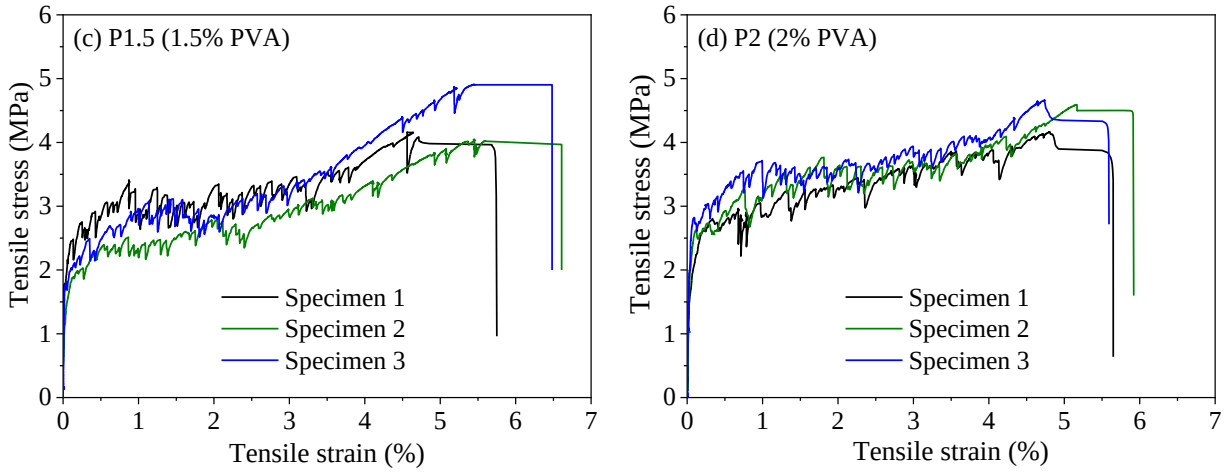

Fig. 10. Tensile stress-strain curves of all mixtures.

3.3.2 Failure patterns

The cracking behaviour is critical for structural design, as the crack control ability of the material contributes to the serviceability and durability of the structures [52]. **Fig. 11** demonstrates the typical failure patterns of SHGC mixtures under uniaxial tension. All cracks were captured right before unloading to avoid difficulties of tracing the cracks due to the possible closure of microcracks when the load was removed [53]. Here, only the tested area within the gauge length (30 × 80 mm) was presented. As expected, all SHGC specimens exhibited multiple micro-cracking behaviour under uniaxial tension, leading to strain-hardening behaviour, while the microcrack features varied with the fibre content in SHGC, which is consistent with the stress-strain curves of the corresponding mixtures shown in **Fig. 10**. Among them, P1 showed the least crack number but wider crack width (142.86 μm) due to the less efficient fibre bridging effect. When the fibre content was increased to 1.5% and 2%, the crack number increased (see **Fig. 11**) while the crack width reduced to 111.35 μm and 85.39 μm, respectively (see **Table 4**), which can be attributed to the more significant fibre bridging effect induced by higher fibre content. Compared with P1.5, the tensile strain of P2 exhibited a marginal reduction of 4.89% on average, while the crack width of P2 dropped by about 23.31% due to the increased fibre bridging effect, leading to more microcracks in P2 under uniaxial tension.

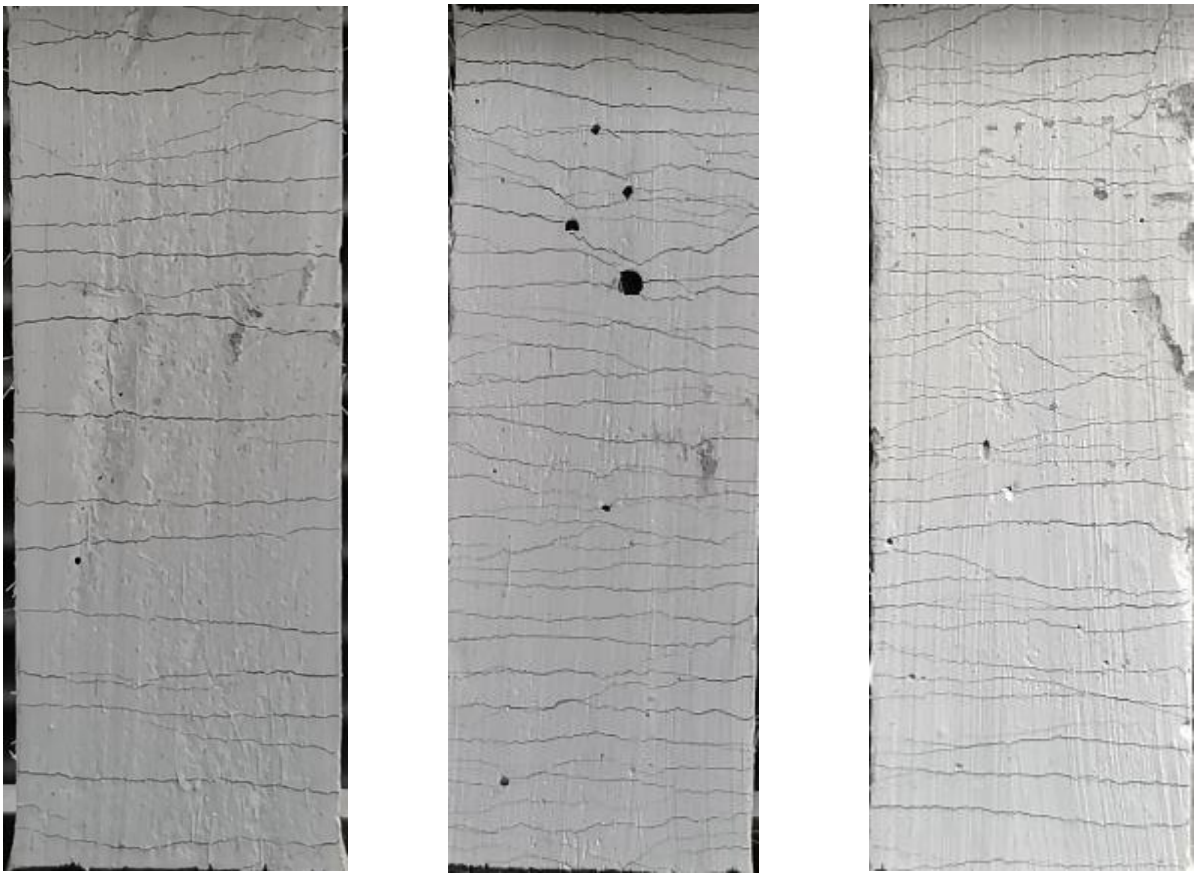

(a) P1 (b) P1.5 (c) P2

Fig. 11. Typical failure patterns of SHGC mixtures.

3.3.3 Tensile strength

Fig. 12 demonstrates the effect of fibre content on the ultimate tensile strength of all mixtures, indicating that the increase of fibre content resulted in a significant enhancement of tensile strength. P0 had a tensile strength of 1.04 MPa, which was improved by 151.25%, 321.35%, and 331.07%, respectively, when adding 1%, 1.5%, and 2% PVA fibres. This agrees with the finding by a previous study [44] that over 100% increase in tensile strength of geopolymer mortar can be achieved by adding 2% PVA fibre. This can be ascribed to the fibre bridging effect, where the number of fibres that provide efficient bridging tends to increase when more fibres are added.

Fig. 13 displays the toughening mechanisms of SHGC specimens, including fibre bridging, fibre rupture and fibre pull-out. Strain-hardening behaviour of SHGC can be attributed to the incorporation of PVA fibres, which limited the initiation and propagation of microcracks because of the fibre bridging effect. Once the bond strength between fibre and matrix was not enough to resist the tensile stress, the fibre pull-out occurred, while the fibre rupture happened when the tensile stress exceeded the tensile strength of PVA fibre.

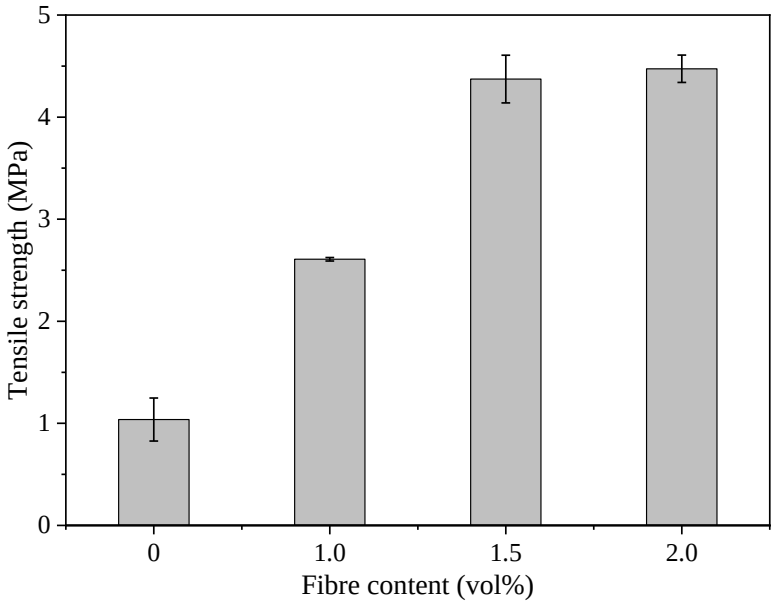

Fig. 12. Effect of PVA fibre content on tensile strength of SHGC.

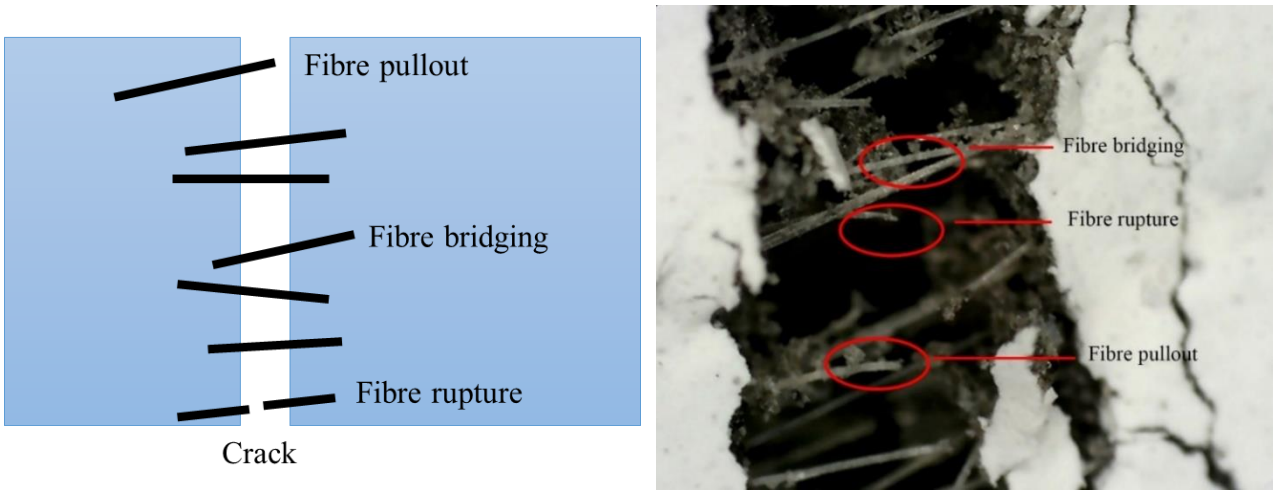

Fig. 13. Toughening mechanisms of SHGC specimens: schematic and digital image.

3.3.4 Micromechanical analysis

As mentioned above, pseudo strain-hardening behaviour requires the satisfaction of two criteria, including strength-based and energy-based criteria. Micromechanical parameters of SHGC mixtures were obtained from uniaxial tension, single-crack tension, and three-point bending tests. **Table 5** presents the single-crack tension test results and micromechanical parameters of P1, P1.5, and P2. It can be observed that the first-crack strength was smaller than peak stress for all mixtures, and the pseudo strain-hardening (PSH) index (J_b'/J_{tip}) of all SHGC specimens exceeds 3, indicating that all mixtures satisfied both the strength-based and energy-based criteria for SHGC [54]. It was demonstrated that the strain-hardening behaviour along with saturated/stable multiple micro-cracking can be achieved only when the PSH index of the composite exceeds 3, and they can be easier to be

achieved when the PSH value is larger [44].

Table 5 Results of single-crack tension test and micromechanical parameters of SHGC mixtures.

Mix No.	Single-crack tension test results			Micromechanical parameters		
	Peak stress (MPa)	Crack opening (mm)	Fibre complementary energy (J/mm^2)	First crack strength (MPa)	Crack tip toughness (J/mm^2)	PSH index
P1	3.21	0.34	219.19	1.13	24.94	8.79
P1.5	3.56	0.27	236.32	1.84	24.94	9.48
P2	4.34	0.44	323.80	2.68	24.94	12.98

3.4 Static compressive behaviour

Fig. 14 shows the typical failure patterns of all cubes under static compression. The incorporation of PVA fibre altered the failure pattern of geopolymer composites from fragile to ductile mode. Geopolymer specimens without fibre failed following the typical fragile failure pattern of normal cementitious materials, i.e., two pyramid failure (**Fig. 14a**), while SHGC specimens containing PVA fibre regardless of fibre content presented the shape integrity up to the end of the test, where a series of cracks can be observed (**Fig. 14b-d**). The change of the failure pattern can be attributed to the bridging effect due to additional fibres, which resist sliding and propagation of cracks and constrain the lateral expansion subjected to compressive load [55, 56]. Similar to cubes, failure patterns of cylinders were changed with the incorporation of PVA fibre. Geopolymer mortar without fibre failed suddenly in a brittle manner, while SHGC specimens showed crushing failure, where shape integrity was retained, and vertical cracks can be observed through specimens surrounding the inner core.

(a) P0 (b) P1 (c) P1. 5 (d) P2

Fig. 14. Typical failure patterns of SHGC cubes.

Fig. 15 displays the compressive strength of all mixtures obtained from cubes and cylinders. It should be mentioned that the compressive strength of all tested cylinders has multiplied a factor (0.82) when the aspect ratio (length-to-diameter ratio) of the specimen is less than 1.75 as per ASTM C39/39M-21 [57]. For cubic specimens, regardless of fibre content, the addition of PVA fibre resulted in a reduction of compressive strength. The geopolymer mortar without fibre (P0) had a compressive

strength of 45.67 MPa. As the PVA fibre content was increased by 1%, 1.5%, and 2%, the compressive strength of geopolymer mortar was reduced by 21.82%, 17.01%, and 28.25%, respectively, which is in consistence with previous studies on geopolymer composites [28, 44, 58] and cementitious composites containing PVA fibres [59, 60]. As mentioned previously, incorporating PVA fibre can avoid the crack extension via bridging the micro-cracks, which improved the integrity of cubic specimens after the compressive failure (**Fig. 14**). However, the compactness of the matrix can be reduced by the presence of fibres as the soft property of PVA fibre (low modulus) may induce more voids [46, 59]. This would lead to a higher extent of compressibility and the local fracture easily appeared around the fibres [46]. Therefore, the compressive strength of SHGC composites is decreased. As seen in **Fig. 15**, the compressive strength of SHGC ranged from 32.77 to 37.90 MPa and P1.5 achieved the highest compressive strength among all SHGC mixtures, while the trend of compressive strength was not consistent with the change of fibre content, which has also been reported in literature [61, 62]. This can be attributed to the different fibre orientation which plays a crucial role in the mechanical properties of SHGC. When the fibres were orientated perpendicular to the cracks induced by compressive loading, the compressive strength tended to be higher. The compressive strength of cylindrical specimens was 5.66-78.98% higher than that of cubic specimens, which can be partially ascribed to the larger region restrained by the loading plate when cylindrical specimens with a 100 mm diameter were used [59]. Besides, the aspect ratio of cylindrical specimens was small (i.e., 0.5) and most of the specimens was under a complex stress state instead of pure tension, resulting in a crushing failure [63, 64]. Thus, the compressive strength was higher. For cylindrical specimens, P0 had a compressive strength of 48.25 MPa. When adding 1%, 1.5%, and 2% PVA fibre, the compressive strength was increased by 13.97%, 3.18%, and 21.54%, respectively. The fibre effect on the cylindrical specimens is different from that on the cubic specimens due to the different compressive failure modes. When the aspect ratio of the tested specimen was increased, the mid-portion of the specimen in pure tension increased [63]. The cubic specimen had a slightly larger aspect ratio than the cylindrical specimen used in this study. Thus, the cubic specimen would fail due to the tensile failure of its mid-portion and the number of effective fibres within this part can significantly affect the final compressive strength of SHGC. Nevertheless, as mentioned early, the failure mode of the cylindrical specimens was different, and more fibres can contribute to influencing the compressive strength.

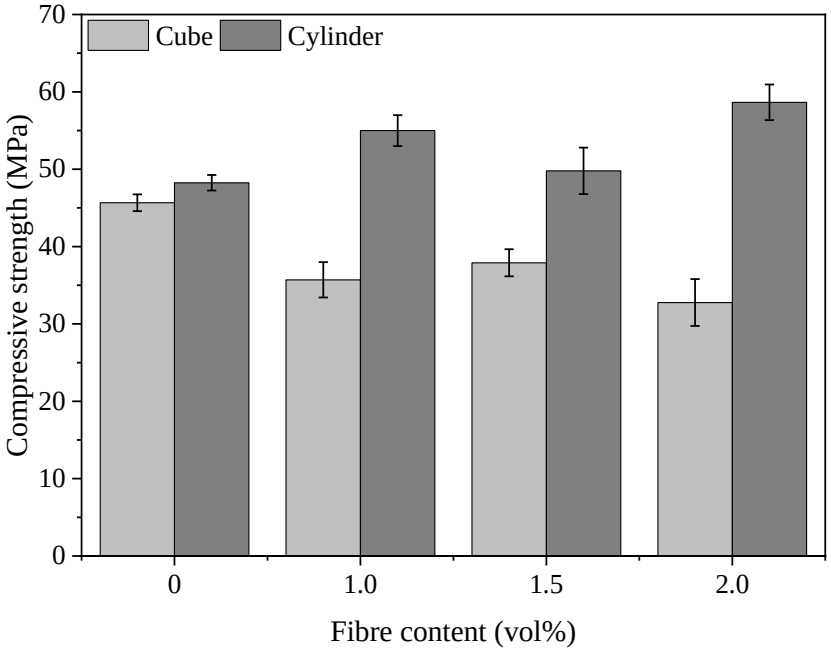

Fig. 15. Compressive strength of SHGC cubes and cylinders with different fibre content.

3.5 Dynamic compressive behaviour

This section presents the results of dynamic compressive behaviour of all mixtures obtained from the SHPB test, including failure patterns, stress-strain response, dynamic compressive strength, DIF, and energy absorption capacity. The dynamic compressive properties of all mixtures in comparison with the corresponding static compressive properties are summarised in **Table 6**.

3.5.1 Failure patterns

Fig. 16 demonstrates the typical failure patterns of all mixtures containing various fibre content at three impact velocities, i.e., 6, 8, and 10 m/s that corresponded to the strain rates of around 50 s^{-1}, 100 s^{-1}, and 150 s^{-1}, respectively. It can be observed that the damage of all mixtures became significant with the increase of strain rates. Geopolymer mortars without fibre (P0) showed pulverised failures under various strain rates (50 s^{-1}-150 s^{-1}), which fractured into large pieces at low strain rates but crushed into fine fragments at high strain rates. At a high strain rate, all specimens including SHGC exhibited pulverised failures. The change of failure patterns with the increasing strain rate was also reported in literature [65-68] that more fragments with smaller sizes were generated when a higher strain rate was applied. Under the high velocity impact, there was very limited time for the cracks to propagate along the path with the lowest cracking resistance. The increased external energy caused by the high velocity impact was consumed by generating more cracks that required higher energy than the propagation of cracks [65, 68].

Regarding the effect of fibre content, compared with P0, the incorporation of PVA fibre altered

the failure patterns of specimens at low and medium strain rates and reduced the damage level of specimens at a high strain rate. At low and medium strain rates, P0 experienced pulverised failures, whereas the specimens containing PVA fibres displayed good integrity until the end of the test with a series of cracks formed on specimens. Apart from the fibre effect, this can also be attributed to the reduced end friction confinement when the grease was applied to the specimens before the dynamic compression. Hence, the splitting vertical cracks occurred throughout the length of the specimen, which initiated from the outer layer [63]. At a high strain rate, although all specimens had pulverised failures, P0 showed a large number of small and irregular broken fragments, while the PVA fibre reinforced SHGC specimens tended to have larger fragments, suggesting that the incorporation of PVA fibre can effectively resist the lateral deformation of specimens under dynamic compression [69]. Besides, at a low strain rate, the specimens containing fibres were not fractured, resulting in a more complete failure pattern [43]. When this happened, the dynamic compressive strength of the specimen tended to be smaller than the static compressive strength, which was also reported in previous studies [66, 70] for polymeric and steel fibre reinforced cementitious composites. This aspect will be explained in more detail below.

Table 6 Summary of static and dynamic compressive properties of all mixtures.

Mix No.	Static compressive strength (MPa)		Average impact velocity (m/s)	Average strain rate (s^{-1})	Dynamic compressive strength (MPa)	Strain at peak stress (με)	Ultimate strain (με)	DIF	Pre-peak (J)	Post-peak energy (J)
	Cube	Cylinder								
			5.84	50.13	49.03	8813	17530	1.02	88.17	106.52
P0	45.67	48.25	7.42	97.55	53.61	19960	28270	1.11	294.18	114.45
			10.51	148.40	83.31	21290	39290	1.73	304.70	339.15
			5.88	51.79	40.06	7918	19160	0.73	57.20	131.02
P1	35.70	54.99	7.88	108.8	47.75	11180	30630	0.87	110.03	270.54
			10.78	174.6	56.72	23730	43320	1.03	256.98	285.64
			5.95	42.59	56.84	9117	15710	1.14	114.77	91.86
P1.5	37.90	49.79	8.34	105.50	70.43	13730	29480	1.41	193.81	297.2
			10.86	145.30	86.87	18930	37100	1.74	305.15	371.68
			5.92	58.14	45.05	8548	17780	0.77	95.70	109.43
P2	32.77	58.65	7.91	80.08	58.55	10780	24600	1.00	128.98	222.85
			10.46	133.80	67.45	16740	32780	1.15	193.54	308.62

Note: DIF is calculated as the ratio of dynamic compressive strength to static compressive strength of cylinder.

Mix No.	Strain rate (s^{-1})		
	50	100	150
P0			
P1			
P1.5			
P2			

Fig. 16. Typical failure patterns of all mixtures under dynamic compression at different strain rates.

3.5.2 Stress-strain response

Fig. 17 shows the dynamic compressive stress-strain curves of all mixtures containing various fibre content under dynamic compression at different strain rates. For all mixtures, the stress-strain curves showed an increasing branch up to the peak stress, followed by a descending branch until the ultimate strain. It is worth mentioning that fibres typically exhibit their bridging effects after the linear ascending stage and a large amount of energy is consumed to pull out or rupture the fibres during this stage [43, 71]. Besides, micro-cracks start to initiate during this stage and visible cracks can be identified along with the crack propagation and coalescence when the peak stress is exceeded [72]. In addition, during this stage, fibres typically experience sliding to overcome the frictional bond or

rupture immediately.

Fig. 18 illustrates the effect of strain rate on the dynamic compressive strength of all mixtures, i.e., the peak stress shown in **Fig. 17**. As the increase of strain rate from a low level (50 s^{-1}) to a medium level (100 s^{-1}) and a high level (150 s^{-1}), the dynamic compressive strength of all mixtures was increased by 9.26-29.97% and 41.59-69.78%, respectively, suggesting that all specimens were sensitive to strain rate. This agrees well with the findings reported in [58, 66, 68, 73, 74]. It can be associated with several factors including the structural effects (lateral inertia effect and end friction confinement effect) [75], viscous effect of free water in voids and pores (known as Stefan effect) [76] and crack initiation and propagation effect [77]. It was found that using the specimens with an aspect ratio of 0.5 can minimise the structural effects [78] and applying the grease on the tested specimens can reduce the end friction effect [79]. In this study, all specimens for dynamic compression test had an aspect ratio of 0.5 and the grease was adopted to both surfaces of the specimens. Hence, the structural effects can be regarded as insignificant while the latter two factors would strongly affect the changes of peak stress with strain rate.

Regarding the effect of PVA fibre on the dynamic compressive strength at different strain rates, increasing the PVA fibre content did not result in a consistent trend, similarly with that of static compressive strength for cubic specimens (**Fig. 15**). P1.5 had the highest dynamic compressive strength, which was 15.83%, 31.37%, and 4.27% higher than that of P0 at strain rates of 50 s^{-1}, 100 s^{-1}, and 150 s^{-1}, respectively. Except P1.5, P1 and P2 exhibited lower compressive strengths than P0 at different strain rates. A similar finding was reported in [58] that the dynamic compressive strength of fly ash-slag based geopolymer was reduced by 16.45-89.42% when the PVA fibre content increased from 0% to 1.2%, which can be attributed to the increasing number of pores and micro-cracks with the increase of PVA fibre content. Additionally, previous studies also found that when the fibre content exceeded a certain value, the dynamic compressive strength of the mixture was weakened due to the increased porosity [66, 80]. As mentioned previously, the dynamic compressive strength tended to be higher when more new cracks were generated rather than the propagation of existing cracks, as the initiation of new cracks would consume more energy. Thus, if more existing cracks appear inside the specimen, the dynamic compressive strength would be reduced. Thus, adding appropriate fibre content is important to avoid fibre clumping or balling, minimise the significant increase of pores and voids, and achieve a better fibre orientation [46]. Similar to static mechanical properties, the fibre orientation is also crucial for dynamic mechanical properties [69, 73], which can vary depending on

the fresh properties, e.g., flowability and rheology [81]. Under a good fibre orientation, fibres can effectively bridge the existing cracks and slow down the crack propagation. Thus, more new cracks would initiate in other areas. Besides, when the strain rate is higher, it requires more energy to fracture the bridging action of fibres as there is no sufficient time for the cracks to grow along the weak paths and thus the dynamic compressive strength would be higher. Based on results of drying shrinkage and static mechanical properties, it seems that P1.5 exhibited better fibre orientation and therefore showed a higher dynamic compressive strength under various strain rates. It should be mentioned that when the strain rate was equal to or smaller than 100 s^{-1}, the dynamic compressive strength of P1 was about 13.17-27.15% smaller than its static compressive strength (54.99 MPa), which can support the previous discussion on the failure patterns (Section 3.5.1) that the specimens were not completely fractured. A similar phenomenon was observed for P2 when the strain rate was around 50 s^{-1}.

Table 6 presents the strain at the peak stress, i.e., peak strain, which can reflect the deformation capacity of the specimens [82]. Consistent with the dynamic compressive strength, the peak strain of all mixtures was increased considerably with the increasing strain rate. For instance, the peak strain for P0 was increased by 126.48-141.57% when the strain rate changed from 50 s^{-1} to higher levels, and it did not show a clear change trend with PVA fibre content. When the strain rate was in the range of 100-150 s^{-1}, P0 exhibited a higher peak strain, while at low strain rates, the peak strain was comparable for all mixtures ranging from 7918 με to 9117 με. All these indicated that the peak strain was sensitive to strain rate instead of fibre content, which is in good agreement with previous studies [68, 69, 72, 73].

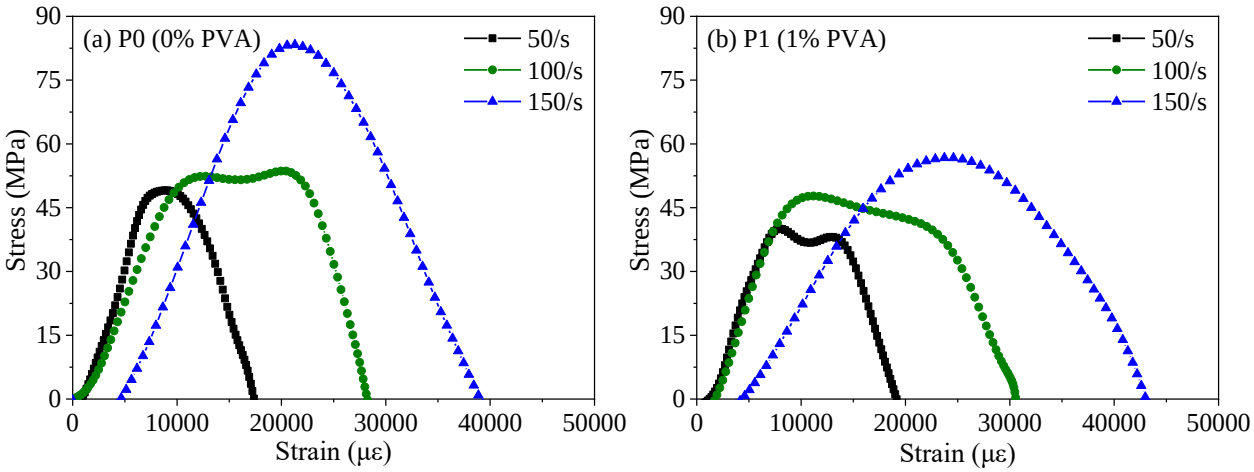

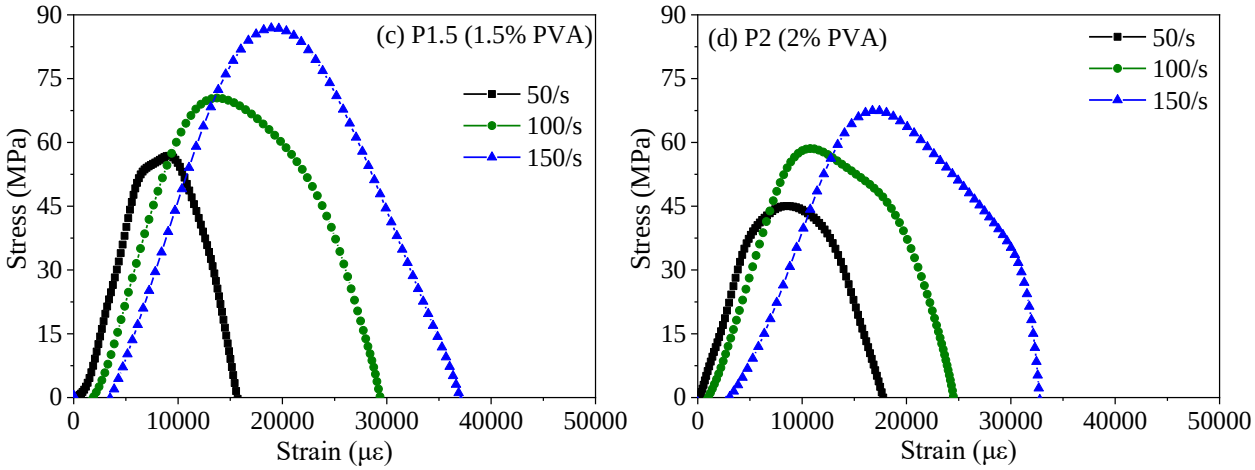

Fig. 17. Dynamic compressive stress-strain curves of all mixtures at different strain rates.

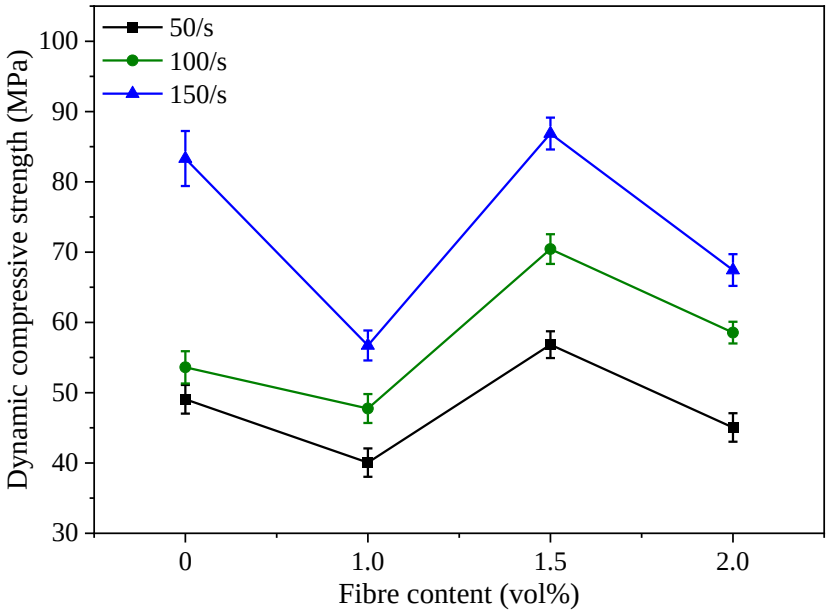

Fig. 18. Dynamic compressive strength of all mixtures under dynamic compression at different strain rates.

3.5.3 Dynamic increase factor (DIF)

DIF is defined as the ratio of dynamic compressive strength to the static compressive strength of the mixture, which has been widely used to evaluate the effect of strain rate on the material properties [41, 43, 72]. In this study, the DIF was calculated as the ratio of dynamic compressive strength to static compressive strength of cylindrical specimen. According to **Table 6**, the DIF values of all mixtures in this study were mostly higher than 1, indicating that the dynamic compressive strength of all mixtures was higher than the static compressive strength. Nevertheless, at some strain rates, P1 and P2 exhibited DIF values less than 1. The possible reasons for this were provided in the previous sections. On the other hand, previous studies indicated that the DIF increased with the log10 of strain rate linearly for quasi-brittle materials, like concrete [65, 83, 84], which can also be observed in this

study as illustrated in **Fig. 19a** that there existed a linear relationship between DIF and strain rate for all mixtures. It can be described using $DIF = b + c\log_{10}(\dot{\varepsilon}_s)$, where b and c are constants and summarised in **Table 7**. The reliability of the fitting curves for all mixtures can be assessed by considering the R^2, where the equations for all SHGC specimens with various fibre content showed high reliability with R^2 close to 1, whereas the fitting linear equation for P0 had slightly less reliability ($R^2 = 0.72$).

The slope (c) of the equation in **Table 7** can reflect the increasing rate of dynamic compressive strength as the increase of strain rate when the intercept (b) is similar. It can be observed that as the strain rate raised, the increasing rates of dynamic compressive strength for P0 and P1.5 were higher than those for P1 and P2. Unlike traditional cementitious materials, the water in the alkaline activator is not reactant and acted as a medium inside the geopolymer mixture [85]. Thus, more free water is available in pores and voids, which would generate a meniscus at the crack tip limiting the crack propagation and thus the dynamic compressive strength would be enhanced [86]. In addition, it was reported that the increasing rate of dynamic compressive strength was higher for concrete with lower quality [87]. As seen in **Fig. 15**, the static compressive strength of P0 (cylindrical specimen) was the lowest, which may explain why the increase of DIF was more sensitive to the strain rate (considering the definition of DIF). For P1.5, although the free water may be reduced due to the hydrophilic behaviour of PVA fibre, the good fibre orientation can provide an effective bridging action, as discussed previously, and thus more energy would be needed to fracture this bridging behaviour along with the generation of more new cracks, resulting in an increased DIF. These can be also seen in **Fig. 19b** that P1.5 had the highest DIF values at different strain rates, ranging from 1.14-1.74. The results of DIF are consistent with that of dynamic compressive strength.

Table 7 Fitted equations of DIF against strain rate for all mixtures.

Mix No.	Fitted equation of DIF	R^2
P0	$DIF = 1.360\log_{10}(\dot{\varepsilon}_s) - 1.377$	0.721
P1	$DIF = 0.611\log_{10}(\dot{\varepsilon}_s) - 0.320$	0.965
P1.5	$DIF = 1.219\log_{10}(\dot{\varepsilon}_s) - 0.957$	0.957
P2	$DIF = 0.793\log_{10}(\dot{\varepsilon}_s) - 0.580$	0.999

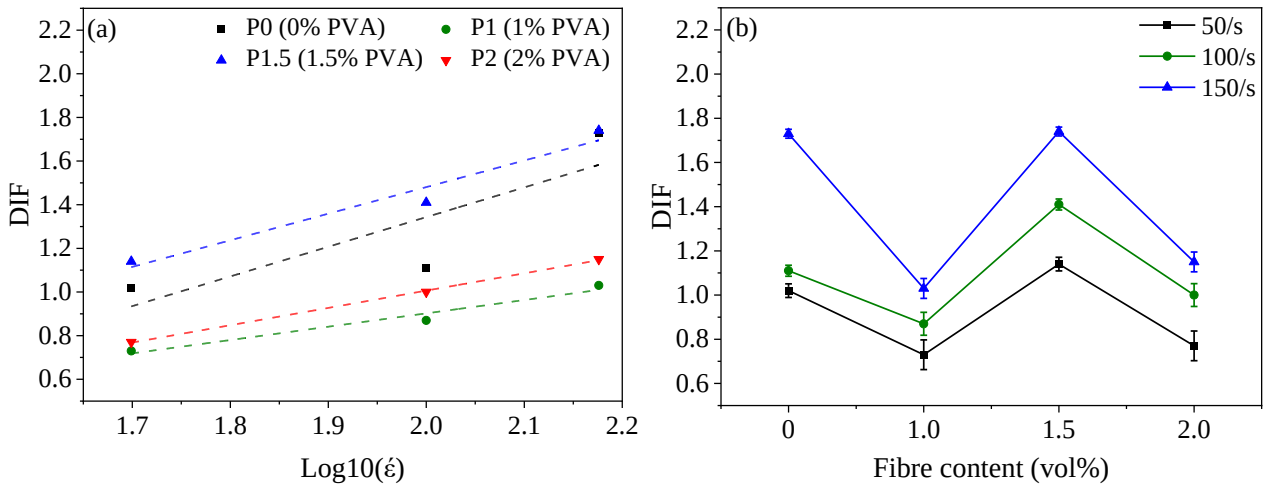

Fig. 19. DIF of all mixtures under dynamic compression at different strain rates.

3.5.4 Energy absorption capacity

The energy absorption capacity of all mixtures was characterised by pre-peak energy and post-peak energy, which are defined as the energy absorbed by the specimen up to the peak stress during the SHPB test and the energy absorbed by the specimen in the post-peak region, respectively [43, 66]. **Fig. 20** shows the fracture energy and post-peak energy of all mixtures calculated based on stress-strain curves presented in **Fig. 17**. Similar to dynamic compressive strength and DIF, both fracture energy and post-peak energy of all mixtures were enhanced significantly by 7.44-349.27% with the increasing strain rate from 50 s^{-1} to 150 s^{-1}, which can be associated with the effects of crack initiation and propagation.

As discussed in Section 3.5.2, the ascending part of the stress-strain curve referred to the initiation of micro-cracks and the fibre pull-out or rupture process, while the descending part related to the crack propagation and complete pull-out or rupture of fibres. This can explain why the post-peak energy of SHGC was mostly higher than the pre-peak energy, suggesting that a large amount of energy was dissipated to pull out or rupture the fibres. For instance, at various strain rates, the post-peak energy of P1.5 was about 11.15-145.88% higher than its pre-peak energy. It is worth noting that when the strain rate was 150 s^{-1}, the difference between them was reduced (only 11.15%) as the high velocity impact may damage the fibres immediately rather than pulling the fibres out. A very big portion of the energy can be absorbed during the pull-out process of fibres. Regarding P0, the difference between the pre-peak energy and the post-peak energy was very small, ranging from 11.31% to 61.10%. Typically, the pre-peak energy of the mixtures containing fibres should be higher than that without fibres, as reported in [66, 68]. However, the pre-peak energy of SHGC was mostly lower than that of geopolymer mortar (except P1.5), as seen in **Fig. 20a**. Xiao et al. [58] observed that the PVA

fibre reinforced geopolymers exhibited lower energy absorption capacity than geopolymer mortars due to the significant reduction in dynamic compressive strength induced by the incorporation of PVA fibre. A similar finding was reported in [73] that the energy absorption capacity of PP fibre reinforced concrete dropped when the PP fibre content exceeded a certain value. The energy absorption capacity can be affected by both dynamic compressive strength and peak strain. As presented in **Table 6**, the fibres did not have an obvious effect on the peak strain and P0 exhibited higher peak strain at strain rates, which can be ascribed to the increased cumulative strain when more cracks were generated [40], as confirmed by **Fig. 16**. As seen in **Fig. 20b**, the post-peak energy of all SHGC mixtures was mostly larger than that of geopolymer mortar when the strain rate exceeded 50 s^{-1} owing to the extra part of the energy required to pull out or rupture the fibres. Nevertheless, due to the reduced dynamic compressive strength, the total absorbed energy (sum of pre-peak energy and post-peak energy) of P1 and P2 was still lower than that of P0. Consistent with dynamic compressive strength and DIF, P1.5 outperformed P0 in terms of total absorbed energy at different strain rates, with an improvement of 6.13-20.16%.

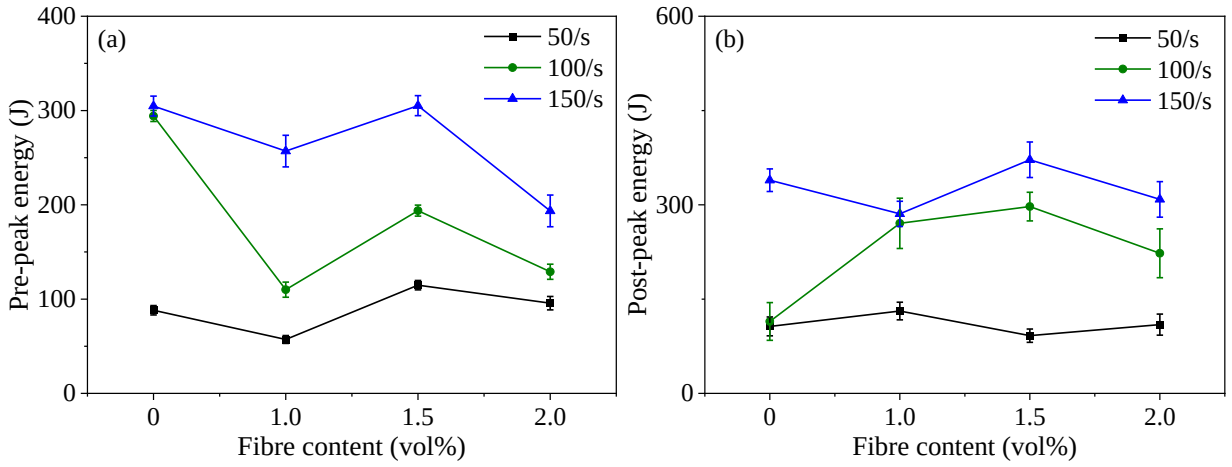

Fig. 20. Energy absorption capacity of all mixtures under dynamic compression at different strain rates: (a) pre-peak energy and (b) post-peak energy.

4. Conclusions

This paper presents a systematic experimental study on the effect of PVA fibre content (0%, 1%, 1.5%, and 2% by volume) on engineering properties of fly ash-slag based strain-hardening geopolymer composite (SHGC), including flowability, drying shrinkage, tensile properties, and compressive properties, focusing on the tensile strain-hardening behaviour and dynamical compressive behaviour. Based on the experimental results, the main conclusions can be drawn as follows:

- Compared to pure geopolymer mortar, the PVA fibre reinforced SHGC specimens had a lower flowability. The addition of up to 2% PVA fibre resulted in a reduction in flowability of fresh mixtures by 26.06% due to the increased shear resistance. The drying shrinkage of SHGC specimens at 28 d declined with the incorporation of fibre content, except for P1.5 (1.5% PVA) that had a smaller drying shrinkage than P2 (2% PVA) due to the relatively weaker fibre-matrix interfacial bond and higher porosity of geopolymer matrix in P2.
- The pure geopolymer mortar exhibited a brittle failure, while all SHGC specimens containing PVA fibre presented a strain-hardening behaviour along with multiple micro-cracking. The addition of 2% PVA fibre resulted in an increase of ultimate tensile strength by 331.07%. The ultimate tensile strain of P1.5 and P2 was approximately 200 times that of P0, which can be ascribed to the fibre bridging effect. All specimens reinforced with PVA fibre fulfilled both the strength-based and energy-based criteria for SHGC, as indicated by the pseudo strain-hardening (PSH) index that ranged from 8.79 to 12.98, exceeding the required PSH index of 3.
- For both cubic and cylindrical SHGC specimens, the failure patterns of them changed with addition of PVA fibre while the integrity was mostly remained. With the increase of fibre content to up to 2%, the static compressive strength of cubic specimens reduced by 28.25%, while that of cylindrical specimens went up by 21.55%, which can be ascribed to their different failure patterns. Compared to cubic specimens, cylindrical specimens had a 5.66-78.98% higher compressive strength owing to the larger region restrained by the confinement and complex stress distribution under loading.
- The strain rate had a significant influence on the compressive behaviour of SHGC. With the increasing strain rate from a low level (50 s^{-1}) to a medium level (100 s^{-1}) and a high level (150 s^{-1}), the dynamic compressive strength of SHGC was increased by 9.26-29.97% and 41.59-69.78%, respectively. The dynamic impact factor (DIF) and energy absorption capacity of all mixtures were also enhanced with the increase of strain rate. There existed a linear relationship between DIF and log10 of strain rate. The dynamic compressive behaviour of SHGC was strongly associated with the fibre content and fibre distribution. P1.5 outperformed other mixtures in terms of dynamic compressive strength, DIF and energy absorption capacity.
- SHGC containing 1.5% PVA fibre can be regarded as the optimal mixture considering the static and dynamic properties.

Acknowledgements

The authors gratefully acknowledge the financial support from the Engineering and Physical Sciences Research Council (EPSRC), UK under Grant No. EP/R041504/1 and the Royal Society, UK under Award No. IEC\NSFC\191417 as well as the Visiting Researcher Fund Program of State Key Laboratory of Water Resources and Hydropower Engineering Science, China under Award No. 2019SGG01.

References

[1] Y.H.M. Amran, R. Alyousef, H. Alabduljabbar, M. El-Zeadani, Clean production and properties of geopolymer concrete; A review, J. Clean. Prod. 251 (2020) 119679.

[2] J. Lehne, F. Preston, Making concrete change: Innovation in low-carbon cement and concrete, The Royal Institute of International Affairs, London, 2018.

[3] A. Bosoaga, O. Masek, J.E. Oakey, CO_2 capture technologies for cement industry, Energy Procedia 1 (2009) 133-140.

[4] J.L. Provis, J.S.J. Van Deventer, Geopolymers: structures, processing, properties and industrial applications, Elsevier, 2009.

[5] K.H. Yang, J.K. Song, K.I. Song, Assessment of CO_2 reduction of alkali-activated concrete, J. Clean. Prod. 39 (2013) 265-272.

[6] N. Ranjbar, M. Mehrali, M. Mehrali, U.J. Alengaram, M.Z. Jumaat, High tensile strength fly ash based geopolymer composite using copper coated micro steel fiber, Constr. Build. Mater. 112 (2016) 629-638.

[7] M. Khalaj, A. Khoshakhlagh, S. Bahri, M. Khoeini, M. Nazerfakhari, Split tensile strength of slag-based geopolymer composites reinforced with steel fibers: Application of Taguchi method in evaluating the effect of production parameters and their optimum condition, Ceram. Int. 41 (2015) 10697-10701.

[8] J.S. Alcaide, E.G. Alcocel, F. Puertas, R. Lapuente, P. Garcés, Carbon fibre-reinforced, alkali-activated slag mortars, Mater. de Construccion 57 (2007) 33-48.

[9] J.L. Vilaplana, F.J. Baeza, O. Galao, E.G. Alcocel, E. Zornoza, P. Garcés, Mechanical properties of alkali activated blast furnace slag pastes reinforced with carbon fibers, Constr. Build. Mater. 116 (2016) 63-71.

[10] A.M. Rashad, The effect of polypropylene, polyvinyl-alcohol, carbon and glass fibres on geopolymers properties, Mater. Sci. Technol. 35 (2019) 127-146.

[11] N. Ranjbar, M. Mehrali, A. Behnia, A.J. Pordsari, M. Mehrali, U.J. Alengaram, M.Z. Jumaat, A comprehensive study of the polypropylene fiber reinforced fly ash based geopolymer, PLoS One 11 (2016) e0147546.

[12] M.M.A.B. Abdullah, A.M. Izzat, M.T. M. Faheem, H. Kamarudin, I. K. Nizar, M. Bnhussain, A.R. Rafiza, Y. Zarina, J. Liyana, Feasibility of producing wood fibre-reinforced geopolymer composites (WFRGC), Adv. Mat. Res. 626 (2013) 918-925.

[13] J. Wei, C. Meyer, Sisal fiber-reinforced cement composite with Portland cement substitution by a combination of metakaolin and nanoclay, J. Mater. Sci. 49 (2014) 7604-7619.

[14] J.I. Choi, B.Y. Lee, R. Ranade, V.C. Li, Y. Lee, Ultra-high-ductile behavior of a polyethylene fiber-reinforced alkali-activated slag-based composite, Cem. Concr. Compos. 70 (2016) 153-158.

[15] M. Ohno, V.C. Li, A feasibility study of strain hardening fiber reinforced fly ash-based geopolymer composites, Constr. Build. Mater. 57 (2014) 163-168.

[16] T. Kanda, V.C. Li, Interface property and apparent strength of high-strength hydrophilic fiber in cement matrix, J. Mater. Civ. Eng. 10 (1998) 5-13.

[17] M. Amran, S. Debbarma, T. Ozbakkaloglu, Fly ash-based eco-friendly geopolymer concrete: A critical review of the long-term durability properties, Constr. Build. Mater. 270 (2021) 121857.

[18] A. Hassan, M. Arif, M. Shariq, Effect of curing condition on the mechanical properties of fly ash-based geopolymer concrete, Sn Appl. Sci. 1 (2019) 1694.

[19] W. Tu, Y. Zhu, G. Fang, X. Wang, M. Zhang, Internal curing of alkali-activated fly ash-slag pastes using superabsorbent polymer, Cem. Concr. Res. 116 (2019) 179-190.

[20] G. Fang, W.K. Ho, W. Tu, M. Zhang, Workability and mechanical properties of alkali-activated fly ash-slag concrete cured at ambient temperature, Constr. Build. Mater. 172 (2018) 476-487.

[21] B. Nematollahi, J. Sanjayan, J. Qiu, E.H. Yang, High ductile behavior of a polyethylene fiber-reinforced one-part geopolymer composite: A micromechanics-based investigation, Arch. Civ. Mech. Eng. 17 (2017) 555-563.

[22] B. Nematollahi, J. Sanjayan, J. Qiu, E.H. Yang, Micromechanics-based investigation of a sustainable ambient temperature cured one-part strain hardening geopolymer composite, Constr. Build. Mater. 131 (2017) 552-563.

[23] F.U.A. Shaikh, A. Fairchild, R. Zammar, Comparative strain and deflection hardening behaviour of polyethylene fibre reinforced ambient air and heat cured geopolymer composites, Constr. Build. Mater. 163 (2018) 890-900.

[24] M. Nedeljković, M. Luković, K. van Breugel, D. Hordijk, G. Ye, Development and application of an environmentally friendly ductile alkali-activated composite, J. Clean. Prod. 180 (2018) 524-538.
[25] Y. Ling, K. Wang, W. Li, G. Shi, P. Lu, Effect of slag on the mechanical properties and bond strength of fly ash-based engineered geopolymer composites, Compos. B. Eng. 164 (2019) 747-757.
[26] A.C.C. Trindade, A.A. Heravi, I. Curosu, M. Liebscher, F.D. Silva, V. Mechtcherine, Tensile behavior of strain-hardening geopolymer composites (SHGC) under impact loading, Cem. Concr. Compos. 113 (2020) 103703.
[27] ASTM C618-19, Standard specification for coal fly ash and raw or calcined natural pozzolan for use in concrete, ASTM International, West Conshohocken, PA, 2019.
[28] Y. Wang, C.L. Chan, S.H. Leong, M. Zhang, Engineering properties of strain hardening geopolymer composites with hybrid polyvinyl alcohol and recycled steel fibres, Constr. Build. Mater. 261 (2020) 120585.
[29] ASTM C1437-15, Standard test method for flow of hydraulic cement mortar, ASTM International, West Conshohocken, PA, 2015.
[30] ASTM C490, Standard practice for use of apparatus for the determination of length change of hardened cement paste, mortar, and concrete, ASTM International, West Conshohocken, PA, 2017.
[31] H. Yokota, K. Rokugo, N. Sakata, Recommendations for design and construction of high performance fiber reinforced cement composites with multiple fine cracks. High Performance Fiber Reinforced Cement Composites; Springer: Tokyo, Japan. 2008.
[32] L.L. Kan, W.S. Wang, W.D. Liu, M. Wu, Development and characterization of fly ash based PVA fiber reinforced Engineered Geopolymer Composites incorporating metakaolin, Cem. Concr. Compos. 108 (2020) 103521.
[33] K. Yu, Y. Wang, J. Yu, S. Xu, A strain-hardening cementitious composites with the tensile capacity up to 8%, Constr. Build. Mater. 137 (2017) 410-419.
[34] M. Ohno, V.C. Li, An integrated design method of Engineered Geopolymer Composite, Cem. Concr. Compos. 88 (2018) 73-85.
[35] ASTM E399-20a, Standard test method for linear-elastic plane-strain fracture toughness of metallic materials, ASTM International, West Conshohocken, PA, 2020.
[36] S. Zhang, V.C. Li, G. Ye, Micromechanics-guided development of a slag/fly ash-based strain-hardening geopolymer composite, Cem. Concr. Compos. 109 (2020) 103510.
[37] ASTM C109, Standard test method for compressive strength of hydraulic cement mortars, ASTM

International, West Conshohocken, PA, 2021.

[38] C.A. Ross, J.W. Tedesco, S.T. Kuennen, Effects of strain rate on concrete strength, ACI Mater. J. 92 (1995) 37-47.

[39] Z. Zhang, D. Kong, G. Gong, X. Chong, Y. WU, Q. Li, B. MENG, Dynamic mechanical behavior of concrete under high strain rate using SHPB, J. PLA Univ. Sci. Technol. 8 (2007) 611-618.

[40] N. Li, Z. Jin, G. Long, L. Chen, Q. Fu, Y. Yu, X. Zhang, C. Xiong, Impact resistance of steel fiber-reinforced self-compacting concrete (SCC) at high strain rates, J. Build. Eng. 38 (2021) 102212.

[41] J. Xiao, L. Li, L. Shen, C. Poon, Compressive behaviour of recycled aggregate concrete under impact loading, Cem. Concr. Res. 71 (2015) 46-55.

[42] W. W. Chen, B. Song, Split Hopkinson (Kolsky) Bar: Design, Testing and Applications, 2011.

[43] Q. Yu, W. Zhuang, C. Shi, Research progress on the dynamic compressive properties of ultra-high performance concrete under high strain rates, Cem. Concr. Compos. 124 (2021) 104258.

[44] H. Zhong, M. Zhang, Effect of recycled tyre polymer fibre on engineering properties of sustainable strain hardening geopolymer composites, Cem. Concr. Compos. 122 (2021) 104167.

[45] M. Farooq, A. Bhutta, N. Banthia, Tensile performance of eco-friendly ductile geopolymer composites (EDGC) incorporating different micro-fibers, Cem. Concr. Compos. 103 (2019) 183-192.

[46] N. Ranjbar, M. Zhang, Fiber-reinforced geopolymer composites: A review, Cem. Concr. Compos. 107 (2020) 103498.

[47] T. Yang, H. Zhu, Z. Zhang, Influence of fly ash on the pore structure and shrinkage characteristics of metakaolin-based geopolymer pastes and mortars, Constr. Build. Mater. 153 (2017) 284-293.

[48] M. Mastali, P. Kinnunen, A. Dalvand, R. Mohammadi Firouz, M. Illikainen, Drying shrinkage in alkali-activated binders – A critical review, Constr. Build. Mater. 190 (2018) 533-550.

[49] N. Ranjbar, S. Talebian, M. Mehrali, C. Kuenzel, H.S. Cornelis Metselaar, M.Z. Jumaat, Mechanisms of interfacial bond in steel and polypropylene fiber reinforced geopolymer composites, Compos Sci Technol 122 (2016) 73-81.

[50] V. Afroughsabet, S. Teng, Experiments on drying shrinkage and creep of high performance hybrid-fiber-reinforced concrete, Cem. Concr. Compos. 106 (2020) 103481.

[51] H. Zhong, E.W. Poon, K. Chen, M. Zhang, Engineering properties of crumb rubber alkali-activated mortar reinforced with recycled steel fibres, J. Clean. Prod. 238 (2019) 117950.

[52] V.C. Li, Engineered Cementitious Composites (ECC): Bendable Concrete for Sustainable and Resilient Infrastructure, Springer, 2019.

[53] B. Nematollahi, J. Sanjayan, F.U.A. Shaikh, Tensile Strain Hardening Behavior of PVA Fiber-Reinforced Engineered Geopolymer Composite, 27(10) (2015) 04015001.

[54] T. Kanda, V.C. Li, Multiple cracking sequence and saturation in fiber reinforced cementitious composites, (1998).

[55] S.J. Choi, J.I. Choi, J.K. Song, B.Y. Lee, Rheological and mechanical properties of fiber-reinforced alkali-activated composite, Constr. Build. Mater. 96 (2015) 112-118.

[56] Y. Wang, Y. Wang, M. Zhang, Effect of micro-silica sand on engineering properties of strain hardening geopolymer composites, J. Build. Eng. 34 (2021) 101951.

[57] ASTM C39/39M-21, Standard Test Method for Compressive Strength of Cylindrical Concrete Specimens, ASTM International, West Conshohocken, PA, United States, 2021.

[58] S.H. Xiao, S.J. Liao, G.Q. Zhong, Y.C. Guo, J.X. Lin, Z.H. Xie, Y. Song, Dynamic properties of PVA short fiber reinforced low-calcium fly ash - slag geopolymer under an SHPB impact load, J. Build. Eng. 44 (2021) 103220.

[59] K. Yu, Y. Ding, Y.X. Zhang, Size effects on tensile properties and compressive strength of engineered cementitious composites, Cem. Concr. Compos. 113 (2020) 103691.

[60] J.X. Lin, Y. Song, Z.H. Xie, Y.C. Guo, B. Yuan, J.J. Zeng, X. Wei, Static and dynamic mechanical behavior of engineered cementitious composites with PP and PVA fibers, J. Build. Eng. 29 (2020) 101097.

[61] B. Zhu, J. Pan, B. Nematollahi, Z. Zhou, Y. Zhang, J. Sanjayan, Development of 3D printable engineered cementitious composites with ultra-high tensile ductility for digital construction, Mater. Des. 181 (2019) 108088.

[62] J. Ye, C. Cui, J. Yu, K. Yu, F. Dong, Effect of polyethylene fiber content on workability and mechanical-anisotropic properties of 3D printed ultra-high ductile concrete, Constr. Build. Mater. 281 (2021) 122586.

[63] S. Wang, M. Zhang, S. Quek, Effect of Specimen Size on Static Strength and Dynamic Increase Factor of High-Strength Concrete from SHPB Test, J. Test. Eval. 39 (2011) 898-907.

[64] J.K. Kim, S.T. Yi, Application of size effect to compressive strength of concrete members, Sadhana 27 (2002) 467.

[65] X. Chen, S. Wu, J. Zhou, Experimental and modeling study of dynamic mechanical properties of cement paste, mortar and concrete, Constr. Build. Mater. 47 (2013) 419-430.

[66] M. Chen, W. Chen, H. Zhong, D. Chi, Y. Wang, M. Zhang, Experimental study on dynamic

compressive behaviour of recycled tyre polymer fibre reinforced concrete, Cem. Concr. Compos. 98 (2019) 95-112.

[67] S. Wang, M.H. Zhang, S.T. Quek, Mechanical behavior of fiber-reinforced high-strength concrete subjected to high strain-rate compressive loading, Constr. Build. Mater. 31 (2012) 1-11.

[68] M.Z.N. Khan, Y. Hao, H. Hao, F.U.A. Shaikh, Experimental evaluation of quasi-static and dynamic compressive properties of ambient-cured high-strength plain and fiber reinforced geopolymer composites, Constr. Build. Mater. 166 (2018) 482-499.

[69] Z. Wu, C. Shi, W. He, D. Wang, Static and dynamic compressive properties of ultra-high performance concrete (UHPC) with hybrid steel fiber reinforcements, Cem. Concr. Compos. 79 (2017) 148-157.

[70] W. Zhang, Y. Zhang, G. Zhang, Static, dynamic mechanical properties and microstructure characteristics of ultra-high performance cementitious composites, J. Sci. Eng. Compos. Mater. 19 (2012) 237-245.

[71] X. Hou, S. Cao, W. Zheng, Q. Rong, G. Li, Experimental study on dynamic compressive properties of fiber-reinforced reactive powder concrete at high strain rates, Eng. Struct. 169 (2018) 119-130.

[72] G.M. Ren, H. Wu, Q. Fang, J.Z. Liu, Effects of steel fiber content and type on dynamic compressive mechanical properties of UHPCC, Constr. Build. Mater. 164 (2018) 29-43.

[73] H. Zhang, L. Wang, K. Zheng, T.J. Bakura, P.G. Totakhil, Research on compressive impact dynamic behavior and constitutive model of polypropylene fiber reinforced concrete, Constr. Build. Mater. 187 (2018) 584-595.

[74] X. Sun, K. Zhao, Y. Li, R. Huang, Z. Ye, Y. Zhang, J. Ma, A study of strain-rate effect and fiber reinforcement effect on dynamic behavior of steel fiber-reinforced concrete, Constr. Build. Mater. 158 (2018) 657-669.

[75] Y. Hao, H. Hao, G.P. Jiang, Y. Zhou, Experimental confirmation of some factors influencing dynamic concrete compressive strengths in high-speed impact tests, Cem. Concr. Res. 52 (2013) 63-70.

[76] P. Rossi, J.G.M. van Mier, C. Boulay, F. Le Maou, The dynamic behaviour of concrete: influence of free water, Mater. Struct. 25 (1992) 509-514.

[77] D. Yan, G. Lin, Dynamic properties of concrete in direct tension, Cem. Concr. Res. 36 (2006) 1371-1378.

[78] L.D. Bertholf, C.H. Karnes, Two-dimensional analysis of the split hopkinson pressure bar system, J. Mech. Phys. Solids. 23 (1975) 1-19.

[79] Q.M. Li, H. Meng, About the dynamic strength enhancement of concrete-like materials in a split Hopkinson pressure bar test, Int. J. Solids. Struct. 40 (2003) 343-360.

[80] J. Lai, W. Sun, Dynamic behaviour and visco-elastic damage model of ultra-high performance cementitious composite, Cem. Concr. Res. 39(11) (2009) 1044-1051.

[81] E.H. Yang, M. Sahmaran, Y. Yang, V.C. Li, Rheological control in production of engineered cementitious composites, ACI Mater. J. 106(4) (2009) 357-366.

[82] W. Li, J. Xu, Impact characterization of basalt fiber reinforced geopolymeric concrete using a 100-mm-diameter split Hopkinson pressure bar, Mater. Sci. Eng. A. 513 (2009) 145-153.

[83] C. A. Ross, J.W. Tedesco, S.T. Kuennen, Effects of Strain Rate on Concrete Strength, Aci Mater. J. 92 (1995) 37-47.

[84] J.W. Tedesco, J.C. Powell, C.A. Ross, M.L. Hughes, A strain-rate-dependent concrete material model for ADINA, Comput. Struct. 64 (1997) 1053-1067.

[85] Y. Ma, G. Ye, The shrinkage of alkali activated fly ash, Cem. Concr. Res. 68 (2015) 75-82.

[86] Q. Fu, Z. Zhang, X. Zhao, M. Hong, B. Guo, Q. Yuan, D. Niu, Water saturation effect on the dynamic mechanical behaviour and scaling law effect on the dynamic strength of coral aggregate concrete, Cem. Concr. Compos. 120 (2021) 104034.

[87] P.H. Bischoff, S.H. Perry, Compressive behaviour of concrete at high strain rates, Mater. Struct. 24 (1991) 425-450.